ACS APPLIED MATERIALS & INTERFACES

www.acsami.org Research Article

Codelivery of $\pi-\pi$ Stacked Dual Anticancer Drugs Based on Aloe-Derived Nanovesicles for Breast Cancer Therapy

Lupeng Zeng, Wanhua Shi, Huaying Wang, Xin Cheng, Tingting Chen, Liang liang Wang, Jianming Lan, Weiming Sun, Meicen Liu, Xi Zhang,* Jing Zhang,* and Jinghua Chen*

Cite This: *ACS Appl. Mater. Interfaces* 2022, 14, 27686−27702 Read Online

ABSTRACT: To overcome the low efficacy of conventional monotherapeutic approaches that use a single drug, functional nanocarriers loaded with an amalgamation of anticancer drugs have been promising in cancer therapy. Herein, aloe-derived nanovesicles (gADNVs) are modified with an active integrin-targeted peptide (Arg-Gly-Asp, RGD) by the postinsertion technique to deliver indocyanine green (ICG) and doxorubicin (DOX) for efficient breast cancer therapy. We presented for the first time that the $\pi-\pi$ stacking interaction can turn the "competitive" relationship of ICG and DOX inside gADNVs into a "cooperative" relationship and enhance their loading efficiency. The dual-drug codelivery nanosystem, denoted as DIARs, was well stable and leakproof, exhibiting high tumor-targeting capability both *in vitro* and *in vivo*. Meanwhile, this nanosystem showed significant inhibition of cell growth and migration and induced cell apoptosis with the combination of phototherapy and chemotherapy. Intravenous administration of DIARs exhibited high therapeutic efficacy in a 4T1 tumor-bearing mouse model and exhibited no obvious damage to other organs. Overall, our DIAR nanosystem constitutively integrated the natural and economical gADNVs, $\pi-\pi$ stacking interaction based on efficient drug loading, and tumor-targeted RGD modification to achieve an effective combination therapy for breast cancer.

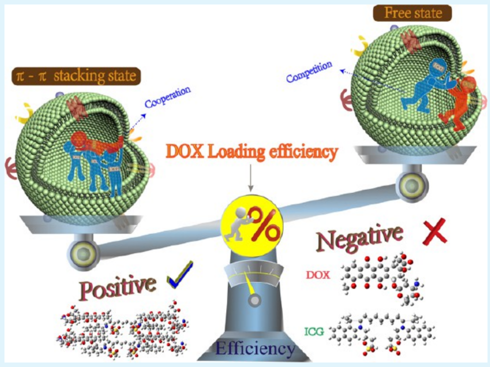

KEYWORDS: *$\pi-\pi$ stacking interaction, aloe-derived nanovesicles, stable and leakproof, targeted drug delivery, breast cancer therapy*

1. INTRODUCTION

Breast cancer as a malignant tumor severely threatens the health of females worldwide.[1] Despite the fact that it is potentially curable in the early stage if without distant metastases, once the metastasis of a breast tumor occurs, its treatment will become tricky and the prognosis can be worsened, eventually affecting the life expectancy of patients.[2] Commonly, chemotherapy is the standard treatment after breast cancer surgery, but the resulting drug resistance of tumor cells usually hinders the progress.[3,4] In addition, it has been reported that the conventional modality of monotherapy that uses a single drug in breast cancer therapy fails to achieve satisfactory therapeutic efficacy.[5] Therefore, combination therapy has been advocated as a new modality of treatment that can potentially enhance therapeutic efficacy.[6] Recently, photothermal therapy (PTT) with the properties of non-invasiveness and high accuracy has obtained great popularity for cancer therapy.[7] Based on the near-infrared (NIR) laser-induced photothermal conversion performance, PTT can generate hyperthermia after NIR stimulation and cause efficient cell ablation.[8] However, PTT shows less effectiveness on the heat-resistant tumor cells, thereby failing to completely eliminate tumor cells.[9] Also, subject to the scope of laser irradiation, the eradication of metastatic tumor cells by PTT is impeded.[10] Thus, a regimen that combines PTT and chemotherapy can likely effectively compensate for the shortcomings of each therapy in breast cancer therapy. However, the rapid clearance of free or unbound drugs and nonspecific distribution in normal organs diminish the clinical curative effect and exert severe toxicity to normal organs, thereby limiting its application.[11]

The development of nanocarrier-based drug delivery systems (NDDSs) effectively ameliorates this problem. Various studies have demonstrated that with the support of nanocarriers, the drug stability and half-life period *in vivo* were enhanced.[12] Additionally, nanocarriers can facilitate drug accumulation at the tumor site *via* the enhanced permeability and retention (EPR) effect of tumors.[13] At present, various nanocarriers have been used in NDDSs, including liposomes,[14] polymeric micelle,[15] mesoporous silica nanoparticles,[16] carbon nanotubes, and metal−organic frameworks.[17] Although these

Received: April 13, 2022
Accepted: May 25, 2022
Published: June 8, 2022

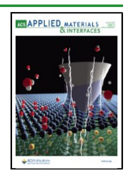

https://doi.org/10.1021/acsami.2c06546
ACS Appl. Mater. Interfaces 2022, 14, 27686−27702

Scheme 1. Preparation of DIARs and Tumor Therapy

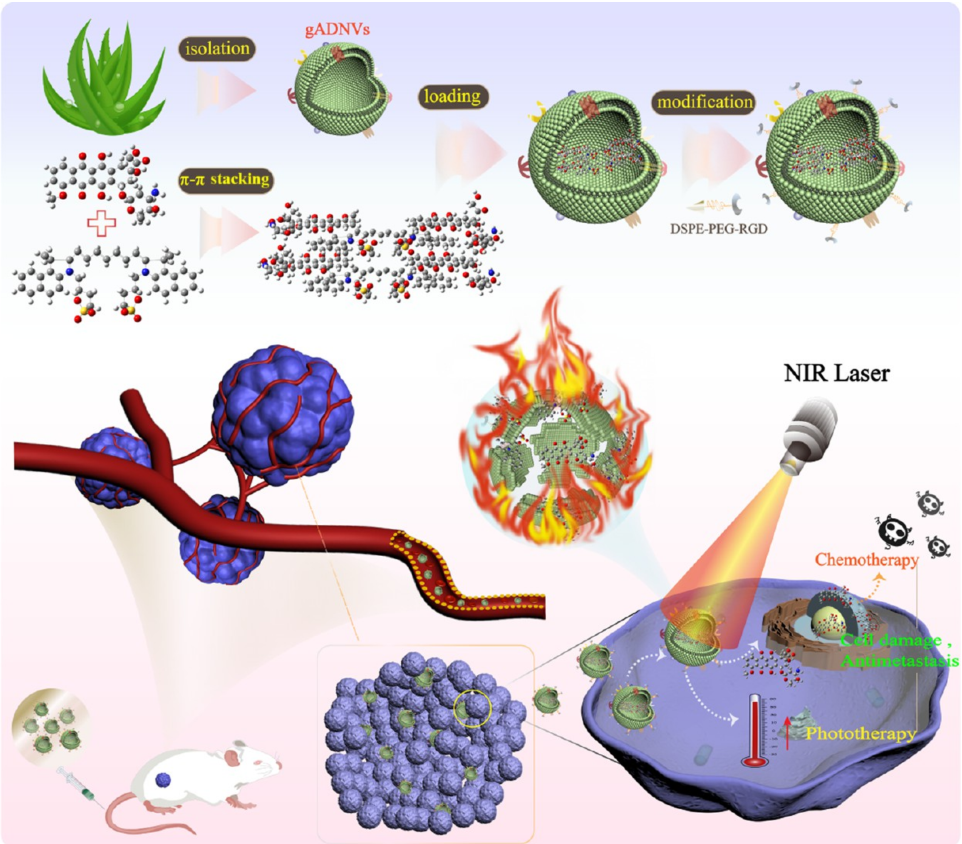

nanocarriers in NDDSs have a number of advantages over conventional dissociative drug delivery, concerns about immunogenicity, toxicity, and complex fabrication process still exist.[18] Recently, plant-derived nanovesicles (PDNVs) as a novel nanocarrier have attracted much attention.[19] Different from synthetic nanoparticles, the natural PDNVs have demonstrated their safety in aspects of organ pathology, hemolytic reaction, and the levels of cellular inflammatory factors.[20−22] Meanwhile, PDNVs are accessible and allow wholesale manufacture.[23] Additionally, the characteristic tropism of PDNVs for particular organs or tissues endows them with targeting capability. Specifically, phosphatidic acid (PA) in PDNVs can be attracted by several bacteria, like *Lactobacillus rhamnosus* and *Porphyromonas gingivalis*, leading to the accumulation of PDNVs at the intestine or gingiva.[24,25] Moreover, PDNVs as vehicles can effectively carry drugs or nanoparticles to bypass the blood−brain barrier (BBB).[26] Therefore, PDNVs with safety, sustainability, and cost-efficiency are promising nanocarriers for developing novel NDDSs.

Our previous study found that aloe-derived nanovesicles (gADNVs) had great structure and storage stability and antioxidant and antidetergent capacity, which was a promising candidate for drug delivery.[27] Herein, we design a NDDS based on gADNVs as nanocarriers. ICG and DOX were loaded into gADNVs to construct a NDDS for a combinatorial photo- and chemotherapy. To achieve the most efficiency, loading sufficiently effective drugs in carriers is a prerequisite.[28] Due to the fixed volume inside the carriers, dual-drug encapsulation can be confined and competitive, resulting in a decrease in drug loading efficiency.[29] Therefore, alleviating the competition between two drugs is challenging yet warranted. A previous study showed that DOX and 10-hydroxycamptothecin could be effectively delivered into cells *via* their $\pi-\pi$ stacking interactions.[30] Since PDNVs, as nanovesicles secreted by plant cells, are composed of a membrane structure similar to cells, it suggests that $\pi-\pi$ stacking interactions presumably may also help in the efficient loading of competitive drugs into PDNVs. Hence, by density functional theory (DFT) calculations and fluorescence spectroscopy, we both theoretically and experimentally demonstrated the $\pi-\pi$ stacking interaction between ICG and DOX, the intensity of which is in a ratiometric manner. The optimal drug loading efficiency of gADNVs was achieved at an ICG/DOX mass ratio of 3:1. The gADNVs were further modified with an integrin-targeted peptide (Arg-Gly-Asp, RGD) *via* the postinsertion technique to endow them with specific tumor-targeting capacity. The obtained nanosystem (denoted as DIARs) was leakproof and protective for ICG and DOX. They showed a great photothermal effect stemming from ICG and caused membrane destruction, which triggered the DOX release for chemotherapy (Scheme 1). The cellular uptake and tumor accumulation results showed that the efficiency of drug delivery improved with RGD modification. The combinatorial antitumor activities of DOX and ICG in DIARs were also determined. Overall, the potential of our prepared DIARs to be a stable and photoresponsive NDDS for breast cancer therapy is well demonstrated and, for the first time, the $\pi-\pi$ stacking interaction of dual drugs for optimal drug loading efficiency is explored. The fact that two drugs work cooperatively, rather than competitively, *via* the $\pi-\pi$ stacking interaction in a ratiometric manner paves the way for the enhancement of

https://doi.org/10.1021/acsami.2c06546
ACS Appl. Mater. Interfaces 2022, 14, 27686−27702

multidrug loading efficiency and provides a promising perspective for the codelivery of multiple drugs in lipid-based carriers.

2. MATERIALS AND METHODS

2.1. Materials. Aloe was purchased from a local flower market. Phosphate buffer (PBS) was purchased from HyClone. Distearoylphosphatidyl ethanolamine-poly(ethylene glycol) 2000-Arginine-Glycine-Aspartate (DSPE-PEG-RGD) with a purity above 99.0% was purchased from Hunan Huateng Pharmaceutical Company Co., Ltd. (Hunan, China). Indocyanine green (ICG) was purchased from Shanghai Macklin Biochemical Co., Ltd. (Shanghai, China). Doxorubicin hydrochloride (DOX·HCl) with a purity above 99.0% was purchased from Beijing Solarbio Science & Technology Co., Ltd. (Beijing, China). Triton X-100 (TX-100) was purchased from Shanghai Macklin Biochemical Co., Ltd. (Shanghai, China). The bicinchoninic acid (BCA) kit was purchased from Thermo Fisher Scientific Co., Ltd. (Shanghai, China). Thiazolyl blue tetrazolium with a purity above 98.0% was purchased from Sigma-Aldrich Co., Ltd. (Shanghai, China). DiO (green) was obtained from Beyotime Biotechnology Co., Ltd. (Shanghai, China). Hoechst 33258 was supplied by Solarbio Technology Co., Ltd. (Beijing, China).

2.2. Cells and Animals. Mouse breast cancer 4T1 cells were provided by the Cell Bank, Chinese Academy of Sciences. 4T1 cells were cultured in Roswell Park Memorial Institute (RPMI, HyClone) with 10% fetal bovine serum (FBS), 1% penicillin, and streptomycin (Thermo Fisher Biochemical Products (Beijing) Co., Ltd.). The cells were cultivated at 37 °C in a humidified atmosphere containing 5% CO_2. BALB/c mice and nude mice (20−25 g) were purchased from Shanghai SLAC Laboratory Animal Co., Ltd. All animal experiments were approved by the Laboratory Animal Management Committee of the Fujian Medical University.

2.3. Preparation and Characterization of DIARs. *2.3.1. Preparation of DIARs.* For DIARs preparation, ICG and DOX were premixed and then incubated with gADNVs in PBS collectively. In brief, 300 μg/mL ICG was mixed with 100 μg/mL DOX and incubated with 200 μg/mL gADNVs (total volume of 1 mL). After incubating for 30 min at 37 °C, a G-25 desalting column was used to filter the solution and remove the DOX and ICG from the free state. Then, the predissolved DSPE-PEG-RGD (using the solution mixed with PBS and methyl alcohol at a ratio of 2:1) was added with a final concentration of 200 μg/mL. After incubation for 30 min, the solution was centrifuged at 100 000*g* for 40 min to remove the uncombined DSPE-PEG-RGD and obtain DIARs. Subsequently, the particle size and morphology of DIARs were characterized by dynamic light scattering (DLS) and transmission electron microscopy (TEM). The methods were the same as the methods used for the characterization of gADNVs, as shown in Methods S1. For drug loading efficiency calculation, DIARs were treated with 10% TX-100, leading to the release of ICG and DOX from gADNVs. An ultraviolet−visible (UV−vis) spectrophotometer (Agilent Technologies) and a fluorescence spectrophotometer (HITACHI, Japan) were used to record the absorbance of ICG and the fluorescence of DOX, respectively.

$$\text{ICG encapsulated efficiency}(\%) = [(A_{\text{ICG in gADNVs after filtration}}/A_{\text{ICG in whole solution without filtration}})] \times 100$$

$$\text{DOX encapsulated efficiency}(\%) = [(F_{\text{DOX in gADNVs after filtration}}/F_{\text{DOX in whole solution without filtration}})] \times 100$$

where A is the absorbance of ICG at 800 nm and F is the fluorescence intensity of DOX at 594 nm.

To investigate the π−π stacking interaction between ICG and DOX molecules, the density functional theory (DFT) calculations were performed to calculate the binding energy (E_b) between ICG and DOX. Density functional theory (DFT) calculations were carried out using the Gaussian 16 program.[31] First, the structures of DOX and ICG were simplified as the models of DOX′ and ICG′ to reduce the computational cost. All of the structures were optimized at the B3LYP/6-31G(d) level to ensure these structures were without imaginary frequencies. Meanwhile, the dispersion correction DFT-D3 introduced by Grimme was employed to consider the long-range interactions in this work.[32] Based on the optimized structures, we calculated the binding energy (E_b) at the B3LYP-D3/6-311G(d,p) level and the solvation model based on electron density (SMD)[33] with water solvent attached was used. The binding energy (E_b) between the DOX′ and ICG′ models is calculated by

$$E_b = E(\text{DOX}') + E(\text{ICG}') - E(\text{complex})$$

where $E(\text{DOX}')$, $E(\text{ICG}')$, and $E(\text{complex})$ are the electronic energies of DOX, ICG, and complex, respectively. All of the dimensional plots of molecular configurations were generated with the GaussView program.[34]

In addition, the π−π stacking interaction between two drugs may affect their fluorescent property. To further verify the π−π stacking interaction between ICG and DOX, a series of ICG/DOX mixed solutions were prepared at different ICG/DOX weight ratios (0:1, 1:1, 2:1, 3:1, 4:1, 5:1), and the fluorescence emission spectra of DOX in these solutions were recorded with a fluorescence spectrophotometer at an excitation wavelength of 488 nm. To ensure the accuracy of the assay, the mixed solutions were rapidly used for detection and completed within 30 min after preparation.

2.3.2. Photothermal Performance of DIARs. The temperature changes of PBS, DOX, ICG, ICG + DOX, and DIARs were monitored with an infrared thermal camera (Shenzhen Laesent Technology Co., Ltd) during laser irradiation for the *in vitro* photothermal performance evaluations. Briefly, the aforementioned solutions (500 μL) with a DOX concentration of 10 μg/mL and/or ICG concentration of 32 μg/mL were irradiated with an 808 nm NIR laser at an optical power density of 1 W/cm^2 for 5 min. Their temperature changes were recorded every 10 s during this period. Moreover, the photothermal performance of DIARs with different concentrations (based on the ICG concentration of 10, 20, 30, 40, 50 μg/mL) was also recorded using the same method. In addition, the morphologic change of DIARs induced by laser irradiation was also observed by TEM.

2.3.3. Laser Irradiation-Controlled DOX Release. Given that the laser irradiation could result in temperature increases and change the membrane permeability of gADNVs or even disrupt their structural integrity, this effect might facilitate drug release from DIARs. Thus, we further investigated the laser irradiation-induced release of DOX in a dynamic process. In brief, 500 μL of DIARs solutions prepared in PBS with a pH of 7.4 was loaded into polypropylene EP tubes and irradiated under a NIR laser (1 W/cm^2) at different times. Concurrently, DIAR solutions with the same concentration and without NIR laser irradiation were prepared in PBS with pH values of 7.4, 6.5, and 5.5 and placed in a shaker at 37 °C with a stirring speed of 200 rpm at different times. At preset time points, the aforementioned solutions were filtered with a G-25 desalting column to obtain DIARs with unreleased DOX. The filtered DIARs were treated with 10% TX-100, and the concentration of unreleased DOX in DIARs was detected with a fluorescence spectrophotometer.

2.3.4. Leakproof Performance and Stability Studies. The drug retention rate of DIARs was monitored in long-term storage. The prepared DIAR solutions (PBS, pH 7.4) were stored at 4 °C for 0, 2, 4, 6, 8, 10, 15, 20, 30, 40, 50, and 60 days. At the preset time points, the solutions of DIARs were filtered using G-25 desalting columns to remove the leaked DOX and ICG. Filtrates were treated with 10% TX-100 and the concentration of ICG and DOX in DIARs were detected with a UV−vis spectrophotometer and a fluorescence spectrophotometer, respectively. The retention of DOX and ICG in DIARs was calculated by

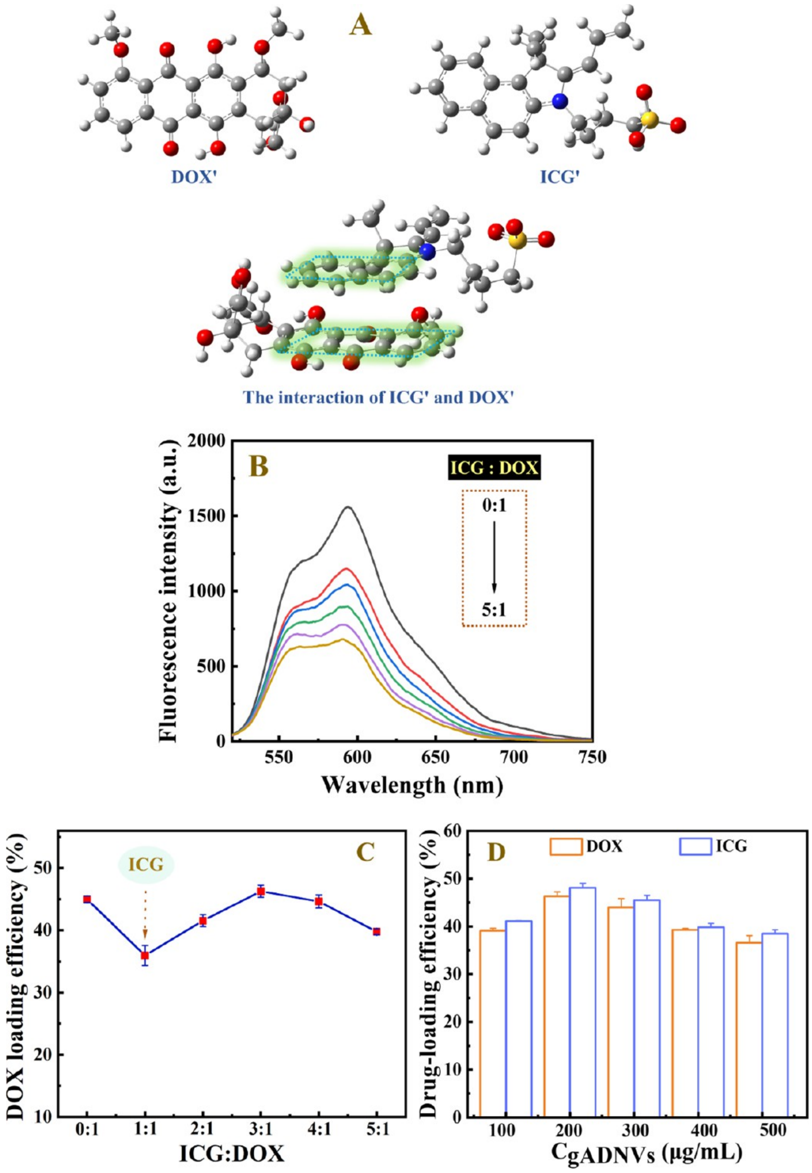

Figure 1. (A) Analysis of the interaction between ICG and DOX by the density functional theory (DFT) calculation. (B) Fluorescence of DOX reduced with the increase of ICG under the $\pi-\pi$ stacking interaction. (C) Loading efficiency of ICG and DOX changed with an increase of ICG. (D) Optimal concentration of gADNVs as carriers for ICG and DOX encapsulation. Data in (C) and (D) are represented as mean values ± standard deviation (SD), n = 3.

$$\text{DOX retention rate}(\%) = (F_{\text{DIARs }(n=i)}/F_{\text{DIARs }(n=0)}) \times 100\%$$
$$, i = 0, 2, 4, 6, 8, 10, 15, 20, 30, 40, 50, 60$$

$$\text{ICG retention rate}(\%) = (A_{\text{DIARs }(n=i)}/A_{\text{DIARs }(n=0)}) \times 100\%$$
$$, i = 0, 2, 4, 6, 8, 10, 15, 20, 30, 40, 50, 60$$

where F is the fluorescence of DOX at 594 nm, A is the absorbance of ICG at 800 nm, and i is the corresponding storage time.

The stability of DIARs was evaluated in serum. Briefly, the free ICG, free DOX, and DIARs with the same concentration were incubated with 70% FBS at 37 °C for 0, 2, 4, 6, 8, 10, 12, 24, 36, 48, and 72 h. At each preset time point, the absorbance of DOX and ICG was detected with a multimode reader (BioTek Instruments, Inc.) with 70% FBS as the blank control. The stability of DIARs was evaluated by recording the change in the relative absorbance (A/A_0, absorbance after reaction/without reaction) of ICG and DOX.

2.4. *In Vitro* Cell Uptake. To investigate the feasibility of cellular uptake to DIARs and the targeted effect of RGD on 4T1 cells, DOX was used as a signal of DIARs to incubate with 4T1 cells and monitored by confocal laser imaging. In brief, 4T1 cells were seeded in a confocal Petri dish (1×10^5 cells/well) until adhered. Then, DIARs (DOX concentration, 10 μg/mL) or free DOX (10 μg/mL) containing RPMI was added to the cell culture cell for 2 or 6 h. At the preset time points, the cells were washed three times with PBS and treated with 2% paraformaldehyde for 15 min to maintain cell morphology. Subsequent cell membrane staining was performed *via* incubating cells with DiO (10 μg/mL) for 15 min. After that, the stained cells were washed three times and stored in sterile PBS solutions and imaged on a TCS SP8 confocal laser scanning microscope (Leica, GER).

2.5. DIAR-Induced Oxygen Free Radicals (ROS) Detection. The 4T1 cells were seeded in 6-well plates at a density of 5×10^5 cells/well. After 12 h, the media were discarded and washed twice with fresh PBS. Subsequently, 2 mL of fresh RPMI was added to each well, in which ICG, DOX, ICG + DOX, and DIARs were diluted to designated concentrations (9.6 μg/mL as ICG, 3 μg/mL as DOX). The test groups were designated as follows: control, ICG, DOX, ICG + DOX, DIARs, ICG + L, ICG + DOX + L, and DIARs + L. "+L"

https://doi.org/10.1021/acsami.2c06546
ACS Appl. Mater. Interfaces 2022, 14, 27686−27702

means plus 808 nm laser irradiation. After 12 h of incubation, the medium was replaced with a fresh medium, and some of these cells were illuminated with an NIR laser (1 W/cm^2, 5 min). After that, the cells were incubated for another 12 h and then incubated with DCFH-DA (10 μM in serum-free medium) for 20 min and detected the intracellular reactive oxygen species (ROS) level by flow cytometry.

2.6. *In Vitro* Cytotoxicity and Apoptosis. The in vitro cytotoxicity of DIARs was explored against 4T1 cells using the 3-(4,5-dimethylthiazol-2-yl)-2,5-diphenyltetrazolium bromide (MTT) assay. The 4T1 cells were seeded in 96-well plates at a density of 1 × 10^4 cells/well. After cell adhesion, the media were discarded and washed twice with fresh PBS. Subsequently, 200 μL of fresh RPMI was added to each well, in which ICG, DOX, ICG + DOX, and DIARs were diluted to designated concentrations. After 12 h, some of these cells were washed and illuminated with an NIR laser (1 W/cm^2, 5 min). The other cells without irradiation were also washed, and the medium was replaced with a fresh culture medium at the same time. All of the cells were further incubated for another 12 h. At a preset time, all cells were treated with the MTT solution (1 mg/mL) for 4 h incubation. Next, the MTT solutions were discarded and dimethyl sulfoxide (DMSO) was added to dissolve the resulting crystals (150 μL/well) and placed on a shaking table at 400 rpm for 10 min for mixing. Then, a microplate reader was used to measure absorbance at a wavelength of 570 nm. In addition, the Calcein AM/PI and Annexin V-FITC/PI staining assays were performed to analyze the apoptosis of 4T1 cells. Briefly, 5 × 10^5 cells/well were seeded in 6-well plates and cultured for 12 h. Then, the RPMI medium was replaced with fresh medium containing drugs. After 12 h of incubation, the cells were washed and replaced with a fresh RPMI medium. Some of the cells were irradiated with an 808 nm laser (1 W/cm^2, 5 min). All cells were incubated for another 12 h. After that, the treated cells were stained with Calcein AM/PI and Annexin V-FITC/PI and then observed with a fluorescence microscope (Leica, Germany) or analyzed by flow cytometry.

To evaluate the antimetastatic effect of DIARs *in vitro*, the scratch assay was performed. The 4T1 cells (5 × 10^5 cells/well) were seeded into 6-well plates and cultured until the cells covered the bottom. The cell monolayer was scratched with a 200 μL pipette tip and washed three times with PBS. Then, fresh RPMI containing different drugs was added and incubated for 12 h. Next, the cells were treated with DOX (5 μg/mL), ICG (16 μg/mL), ICG and DOX (ICG and DOX concentrations of 16 and 5 μg/mL), and DIARs (ICG and DOX concentrations of 16 and 5 μg/mL) with or without NIR laser irradiation (1 W/cm^2, 5 min). After further incubation for 12 h, the cells were rinsed three times with PBS, the scratch of each well was observed with an optical microscope, and the wound area of the scratch was measured by ImageJ.

2.7. *In Vivo* Distribution and Imaging. The ICG-loaded NIR probe in DIARs was used as a tracer to monitor the *in vivo* delivery and distribution of DIARs. In brief, DIARs, free ICG, and ICG-loaded gADNVs (ICG/gADNVs) were intravenously injected into 4T1 tumor-bearing mice (tumor volume 100−150 mm^3) at an ICG dose of 0.5 mg/kg. The fluorescent images of mice were captured with an IVIS Spectrum Imaging System (PerkinElmer, USA) at the preset time points of 6, 12, 24, and 48 h. After 48 h of injection, the mice were sacrificed, and the organs and tumors of each group were observed.

$$\text{tumor volume} = [a \times b^2]/2$$

where a and b are the length and width of the tumor.

2.8. *In Vivo* Antitumor Evaluation. The 4T1 cells (5 × 10^6 cells/mL) were subcutaneously injected to build the tumor-bearing mice models. After 7 days of inoculation of tumor with a tumor volume of 100 mm^3 approximately, mice were randomly divided into eight groups (n = 5) and treated with PBS, ICG, DOX, ICG + DOX, DIARs, ICG plus irradiation (ICG + L), ICG + DOX plus irradiation (ICG + DOX + L), and DIARs plus irradiation (DIARs + L). The NIR laser irradiation (1 W/cm^2, three cycles, 5 min/cycle) was performed at 24 h of administration. The administrations were repeated seven times once every 2 days during the therapeutic period. In the meantime, the tumor volume and body weight of mice were recorded every 2 days. After 21 days, the mice were sacrificed, the tumors and main organs were excised, washed twice with PBS, fixed with tissue fixative fluid, embedded in paraffin blocks to prepare sections, and subjected to immunohistochemical staining. All samples were observed with an optical microscope.

2.9. Statistical Analysis. Data were analyzed at least three times and expressed as the mean values ± standard deviation. Statistically significant differences between groups were evaluated using two-tail paired Student's t-tests. P values less than 0.05 were regarded as statistically significant (ns, no significance, *p < 0.05, **p < 0.01, ***p < 0.001, ****p < 0.0001).

3. RESULTS AND DISCUSSION

3.1. Preparation and Characterization of DIARs. We hypothesize that the $\pi-\pi$ stacking interaction between the two drugs can promote drug loading. As a proof of concept, the density functional theory (DFT) calculations were performed to calculate the binding energy (E_b) between ICG and DOX (Figure 1A). The structures of ICG and DOX were simplified as ICG′ and DOX′, as shown in Figure 1A, to facilitate the calculation. The calculated E_b between ICG′ and DOX′ was 1.427 ev (>0) (the calculation of E_b is shown in Table S1), which indicated that ICG and DOX were tightly bound (Cartesian coordinates are displayed at the end of the Supporting information).[35] And, the $\pi-\pi$ stacking interaction adopts a face-to-face geometry. Experimentally, we further verified this interaction between ICG and DOX by monitoring the fluorescence of DOX. We found that the fluorescence of DOX was reduced with an increase of ICG (Figure 1B), which was consistent with the report that the $\pi-\pi$ interaction could result in decreased fluorescence.[36] Also, this result indicated that the increase in the ratio of ICG and DOX could enhance their $\pi-\pi$ stacking interaction. Thus, we explored the drug loading efficiency of varying ratios of ICG and DOX to evaluate the impact of the $\pi-\pi$ interaction. As shown in Figure 1C, the loading efficiency of DOX was about 45% when loaded alone, but it decreased drastically (dropped to 35%) when the same amount of ICG (nominal ICG/DOX mass ratio, 1:1) was added. It is most likely because ICG competed with DOX for the finite space inside vesicles. Encouragingly, as the dosage of ICG increased with a fixed dosage of DOX, the loading efficiency of DOX increased gradually up to 46%, where the dosage of ICG was three times that of DOX (even higher than the initial DOX loading efficiency without ICG addition). This indicated that the $\pi-\pi$ stacking interaction between ICG and DOX was beneficial to facilitate their loading. We reasoned that the $\pi-\pi$ stacking interaction allowed the two drugs to be orderly stacked and packed, rather than stochastically dissociative; therefore, the space utilization efficiency of vesicles was improved. This finding that the $\pi-\pi$ stacking interaction turns the competitive relationship of multidrug inside carriers into a cooperative relationship paves the way for the subsequent studies in multidrug delivery. In addition, the $\pi-\pi$ stacking interaction was deemed to improve the stability of nanoparticles,[37] and the slight molecular structure change *via* $\pi-\pi$ conjugation may enable the released drugs to escape from the recognition of efflux pumps in the cells.[30] This might be equally beneficial in our prepared DIARs for *in vivo* delivery. Interestingly, when the dosage of ICG exceeded three times that of DOX (ICG/DOX > 3:1), the DOX loading efficiency stopped the enhancement and started declining. It probably resulted from the excessive drugs exceeding the loading capacity of gADNVs. In some cases, overloading drugs

https://doi.org/10.1021/acsami.2c06546
ACS Appl. Mater. Interfaces 2022, 14, 27686−27702

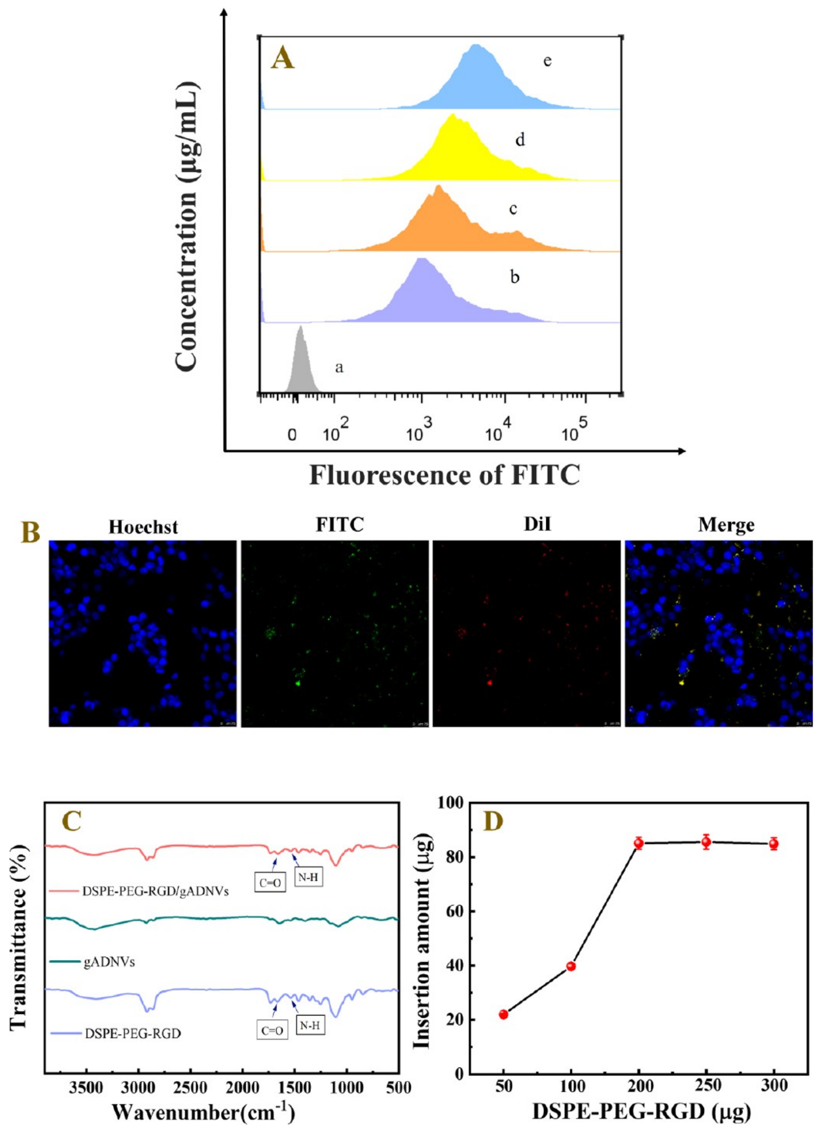

Figure 2. (A) Determination of different concentrations of DSPE-PEG-FITC inserted into gADNVs by flow cytometry: (a) gADNVs without any treatment, (b−e) gADNVs incubated with DSPE-PEG-FITC at concentrations of 30, 50, 100, and 200 μg/mL, respectively. (B) Characterization of the colocation of DSPE-PEG and gADNVs *via* confocal laser microscopy imaging. Hoechst (blue): the nuclear staining channel; FITC (green): the DSPE-PEG channel; DiI (red): the gADNVs staining channel. (C) RGD-modified gADNVs analyzed by Fourier transform infrared spectroscopy. (D) Amount of RGD insertion into gADNVs evaluated with the FITC-labeled DSPE-PEG-RGD using a fluorescence spectrophotometer. Data in (D) are represented as mean values ± SD, n = 3.

would damage the membrane integrity and lead to drug release.[38] Thus, controlling the ratio of ICG and DOX at 3:1 was optimal for their loading into gADNVs in our study.

In addition to the drug proportion, the dosage of lipid carriers also affected drug loading efficiency.[39] To investigate the optimal dosage of carriers, different amounts of gADNVs were used for incubating with DOX and ICG of a fixed amount. As shown in Figure 1D, increasing the concentration of gADNVs at the lower range effectively facilitated the drug loading, and at 200 μg/mL protein concentration of gADNVs, the loading efficiency of both DOX and ICG was simultaneously the maximum. This is reasonable since the void volume inside the vesicles was increasingly larger as we added more vesicles[40] and promoted drug encapsulation. However, when the concentration of gADNVs increased to more than 200 μg/mL, the loading efficiency of ICG and DOX started to decrease. This is possibly because the diffusion of gADNVs in the solution was affected by the increased concentration, which is closely related to drug loading. Previous research showed that passive drug loading (the method in our study) was a dissolution−diffusion process where the diffusion of nanocarrier was an essential factor.[41] As previously reported, the diffusion of a high concentration of lipid nanoparticles was restricted and then influenced the effective drug loading.[42,43] Thus, it was reasonable to predict, in our case, that a higher concentration of gADNVs resulted in a decrease of diffusivity and eventually influenced the loading efficiency. After determining the optimal amounts for drugs and carriers, DSPE-PEG-RGD was post-inserted onto gADNVs to prepare DIARs.

Postinsertion technology can modify the preformed vesicles through hydrophobic interactions and has been widely used in lipid nanocarrier modification.[44] To verify the feasibility of postinsertion of DSPE to gADNVs, the FITC-labeled DSPE-

https://doi.org/10.1021/acsami.2c06546
ACS Appl. Mater. Interfaces 2022, 14, 27686−27702

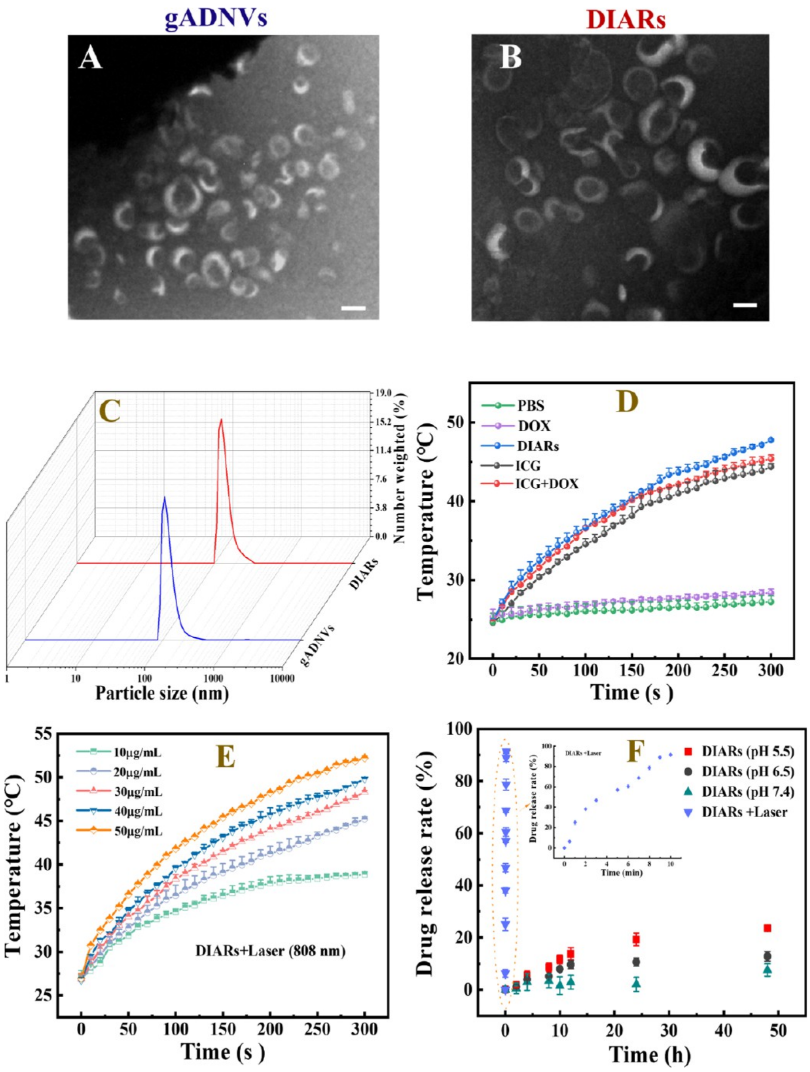

Figure 3. (A) Morphological characterization of gADNVs by TEM. Scale bar is 100 nm. (B) Morphological characterization of gADNVs by DIARs. Scale bar is 100 nm. (C) Characterization of gADNVs and DIARs by DLS. (D) Temperature rise assay under laser irradiation. (E) Temperature rise of DIARs with different concentrations under laser irradiation. (F) DOX release from DIARs under different stimulus conditions. Data in (D), (E), and (F) are represented mean values ± SD, n = 3.

PEG was used to incubate with gADNVs and their fluorescence change was monitored by flow cytometry. As shown in Figure 2A, under the constant concentration of gADNVs and incubating time, as the concentration of DSEP-PEG-FITC increased, the fluorescence of gADNVs enhanced along, suggesting the increased DSPE inserted onto gADNVs. To ensure visual evidence of the insertion of DSPE into gADNVs, the colocation imaging of gADNVs (DiI labeled) and DSEP-PEG-FITC was further performed. Considering that it was difficult to achieve colocalization when vesicles were in a flow state, the preprepared vesicles were fixed after cellular uptake. As shown in Figure 2B, a number of fluorescent spots were found in the cytoplasm, and the overlay of green (FITC) and red (DiI) channels were merged as yellow, suggesting the successful insertion of DSPE into gADNVs. These results confirmed that the postinsertion technique *via* hydrophobic interactions between DSPE and the lipid rafts of gADNVs was feasible for the modification of integrin-targeted peptide RGD onto gADNVs. Subsequently, the RGD-modified gADNVs were further analyzed by Fourier transform infrared spectroscopy (FTIR). As shown in Figure 2C, the FTIR spectrum of DSPE-PEG-RGD/gADNVs exhibited two characteristic peaks of RGD located at 1662 and 1540 cm^{-1}, which were assigned to the C═O and N−H stretching vibrations of amide.[45,46] Then, the FITC-labeled DSEP-PEG-RGD was used to investigate the insertion amount of DSEP-PEG-RGD into gADNVs. As shown in Figure 2D, the amount of DSPE-PEG-RGD inserted into gADNVs increased with the initial incubation dosage added and reached a plateau at a dosage of 200 μg. The insertion rate of DSPE-PEG-RGD was 43.92% at a dosage of 200 μg, which was 85.09 μg of DSPE-PEG-RGD inserted into gADNVs, *i.e.*, 0.43 μg of DSPE-PEG-RGD insertion per microgram of gADNVs. Thus, the results indicated that RGD was modified onto gADNVs successfully.

Next, the morphology, particle size, and ζ potential of prepared DIARs were characterized. TEM images (Figure 3A,B) showed that gADNVs and DIARs exhibited a similar saucer- or cuplike bilayer membrane and remained intact, demonstrating that the encapsulation of DOX and ICG did not affect the integrity of gADNVs. Dynamic light scattering analysis showed that the mean particle diameters were 137.4 ± 9.6 and 141.0 ± 6.8 nm, respectively, with narrow size

https://doi.org/10.1021/acsami.2c06546
ACS Appl. Mater. Interfaces 2022, 14, 27686−27702

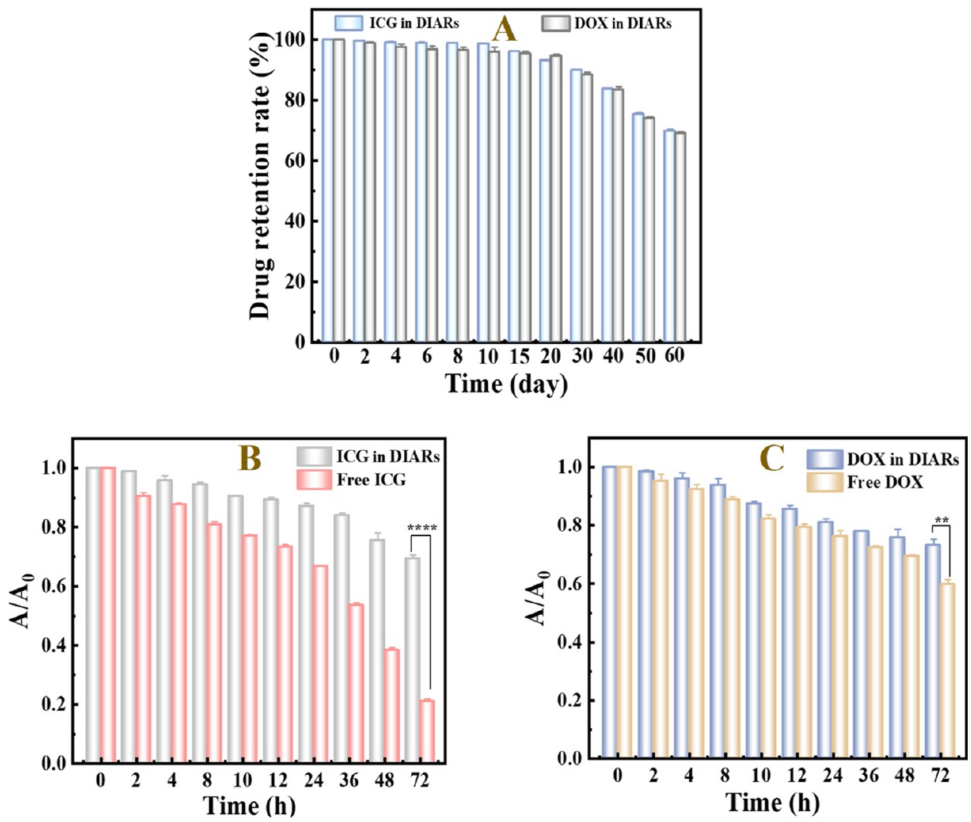

Figure 4. (A) ICG and DOX retention rate in DIARs monitored during long-term storage. (B) Degradation of ICG in DIARs or in the free state during the reaction in serum. A/A_0 is the absorbance ratio of ICG before and after the reaction. (C) Degradation of DOX in DIARs or in the free state during the reaction in serum. A/A_0 is the absorbance ratio of DOX before and after the reaction. Data in (A), (B), and (C) are represented as mean values ± SD, n = 3. Statistical differences were analyzed by a two-tailed Student's *t*-test. $^{**}p < 0.01$, $^{****}p < 0.0001$.

distribution (Figure 3C). This is in accordance with the requirement of enhanced permeability and retention effect (EPR) (particle size < 150 nm),[47] which is beneficial to *in vivo* cancer therapy. The ζ potentials of gADNVs and DIARs were −6.6 and −7.5 mV, respectively, and this slight negative charge of nanoparticles is usually favorable in *in vivo* delivery. Thus, the size and ζ potential of our prepared DIARs are appropriate and promising for cancer therapy.

To investigate the photothermal performance of DIARs, the temperature changes of PBS, DOX, ICG, ICG + DOX, and DIARs were monitored with NIR laser irradiation *in vitro*. Under irradiation at 1 W/cm^2 for 5 min, the temperatures of ICG, ICG + DOX, and DIARs visibly increased to 44.4, 45.4, and 47.8 °C, while PBS and DOX exhibited little change (Figure 3D). Ulteriorly, the DIARs with different concentrations were irradiated with an NIR laser and the effect of DIAR concentration on temperature was monitored. As shown in Figure 3E, the postirradiation temperature increased in a concentration-dependent manner. The results indicated that mixing with DOX or encapsulation into gADNVs did not influence the photothermal performance of ICG. Additionally, the elevated temperature of the thermosensitive DIARs most likely disrupted the membrane structure of gADNVs or enhanced the permeabilization of the membrane, leading to a faster DOX release after laser irradiation. As shown in Figure S1, after laser irradiation, the membrane structure of DIARs changed or ruptured evidently. Then, the laser irradiation-induced release of DOX from DIARs was explored. We prepared DIARs in acidic (pH 5.5 and pH 6.5) buffer for comparison since the intracellular environment was acidic[48] and prepared DIARs in neutral (pH 7.4) buffer without laser irradiation as the blank. As shown in Figure 3F, DIARs exhibited a significant irradiation-dependent release (91.4% release after 10 min irradiation) compared to acid-induced groups (23.6% release in pH 5.5 buffer and 12.8% release in pH 6.5 buffer after 48 h of incubation) and the blank group (7.6% release after 48 h of incubation). This suggested that DIARs were relatively stable under physiological conditions (pH 7.4, 37 °C) and with laser-responsive drug-release performance, which could serve as a controllable system for drug delivery.

For *in vivo* delivery, the stability of nanocarriers is important.[49] Drug retention in nanocarrier during storage is one of the commonly used indicators for stability evaluation.[50] As our previous study showed, gADNVs were rich in a variety of components that were antioxidant or conducive to an ordered phospholipid arrangement, which was beneficial to maintaining their stability.[27] Here, the stability of DIARs was evaluated in PBS, H_2O, and RPMI 1640 culture medium first. As shown in Figure S2, the particle size of DIARs barely changed in PBS and RPMI 1640 after storing for 10 days, even though its particle size increased in H_2O gradually, which indicated that DIARs were stable under physiological conditions during the 10-day storage. Then, the drug retention rate of DIARs was monitored during long-term storage. As shown in Figure 4A, ICG and DOX loaded in DIARs showed nearly equal drug retention rates, both of which remained about 90% after 30 days of storage and about 70% after 60 days of storage. The efficient retention of ICG and DOX in gADNVs might be due to the protective lipid layer of gADNVs. It is worth noting that plasma proteins or enzymes could interfere with nanocarriers, inducing drug leakage ahead of schedule.[51] Thus, the stability of DIARs was further investigated in serum. The ratio of absorbance before and after the reaction (A/A_0) was calculated to evaluate the degradation of drugs in serum. As shown in Figure 4B,C, the A/A_0 ratios of both free ICG and free DOX decreased rapidly during 72 h monitoring, especially for the free ICG, indicating that they were vulnerable to degradation by enzymes or other factors in serum. However, ICG and DOX were more protected from degradation in DIARs. The A/A_0 ratios of both ICG and DOX in DIARs were statistically significantly higher than their free counterpart. These results indicated that DIARs had great stability in storage and in serum, which could avoid the premature release of drugs and was beneficial to *in vivo* delivery.

3.2. *In Vitro* Cell Uptake Study. Cellular uptake is an intuitive means for investigating drug delivery efficiency.[52] Commonly, the luminescent property is necessary for nanoparticles to explore their uptake by cells. In our study, DOX has fluorescence properties. Thus, we used DOX as the tracer for the observation of the cellular uptake of DIARs. As shown in Figure 5A, after incubating with DIARs and free DOX for different periods of time, different intensities of the fluorescence signal of DOX appeared in the nucleus of 4T1 cells. Compared with the free DOX-treated group, more fluorescence was located in 4T1 cells after DIAR incubation. In particular, the red fluorescence of DOX was observed around the cells after incubating with DIARs for 2 h, and the red signal overlaid with the green fluorescent signal of marked cell membranes (see close-up images in Figure S3). Given that the DOX used here was synergistic hydrophilic doxorubicin hydrochloride (DOX·HCl),[53] whereas the cell membrane was a hydrophobic structure,[54] free DOX was not expected to remain on the cell membrane, which was consistent with our result that there was no red fluorescence on the cell membrane in free DOX-treated cells. Thus, the red fluorescence of DOX on cell membranes in the DIARs-treated group must result from the binding of RGD and integrin on the cell surface. We reasoned that this was an intermediate state in which DIARs were targeted to the cell surface through RGD before being fully internalized. And due to the targeting capability of RGD, more DIARs recognized and bound to cells, leading to an increasing internalization of DIARs and thereby an increased fluorescence of DOX. In addition, the uptake of DOX by 4T1 cells was in a time-dependent manner, especially in the DIAR treated group. As shown in Figure 5B, compared with the free DOX-treated group, the fluorescence of DOX increased 1.81- and 2.04-fold, respectively, in the DIARs group after incubating for 2 and 6 h. All of these results indicated that DIARs enabled the favorable delivery of drugs to cells, which offers the potential to improve drug delivery efficiency *in vivo*.

3.3. DIAR-Induced ROS Detection. To investigate the activity of intracellular ROS after treatment with DIARs plus laser, 4T1 cells were treated under different conditions and DCFH-DA was used as a probe to indicate the intracellular ROS level. As shown in Figure S4, no obvious generation of ROS in the control and ICG-treated groups were found, whereas varying degrees of ROS generation were found in other groups. In general, the groups with laser irradiation induced significantly more ROS generation compared with those without laser irradiation. In particular, the DIARs + L-treated group had the highest ROS generation overall. The

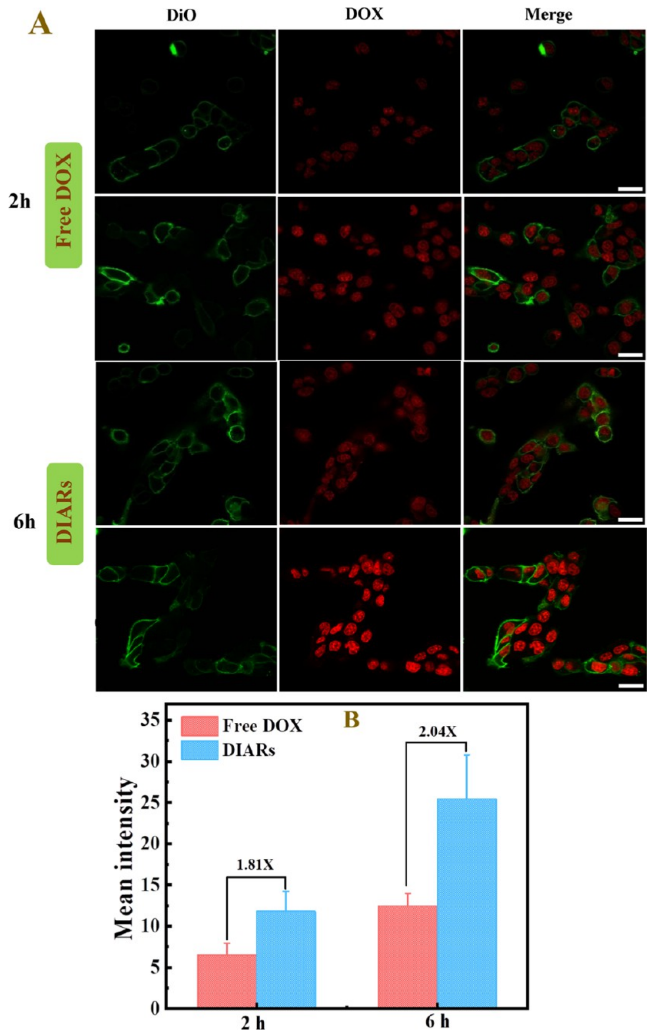

Figure 5. (A) Cell uptake of DIARs analyzed with a laser scanning confocal microscope. DiO (green) is the cell membrane staining channel; DOX is the channel of DIARs. Scale bar is 25 μm. (B) Mean fluorescence intensity of DIARs and DOX quantified by LAS-AF-Lite_2.6.0. Data in (B) are represented as mean values ± SD, n = 3.

ROS generation by DIARs under laser irradiation mainly comes from the photodynamic reaction of ICG and the metabolism of DOX.[55] Therein, ICG promotes the catalyzation of hydrogen peroxide and oxygen under laser irradiation, while the metabolism of DOX activates NADPH oxidase, both of which jointly accelerate the production of ROS. This result indicated that DIARs plus laser could promote ROS generation strongly and may be beneficial to the increase of therapeutic effect.

3.4. *In Vitro* Cytotoxicity and Apoptosis. Next, the cytotoxicity of DIARs was evaluated by the MTT assay against 4T1 cells. For comparison, the cytotoxicity of DOX, ICG, ICG + L, ICG + DOX, ICG + DOX + L, DIARs, and DIARs + L was investigated. For single DOX chemotherapy, the 4T1 cells were treated with DOX in different concentrations, and it showed about 80% cell damage at a concentration of 10 μg/mL (Figure S5). For ICG-based PTT, the cells were treated with or without irradiation. As shown in Figure 6A, ICG exhibited negligible cytotoxicity after incubating with 4T1 cells for 24 h. However, when laser irradiation was applied, the cytotoxicity of ICG was dose-dependent. At a concentration of 32 μg/mL ICG, cell viability decreased from 98.49 to 39.68%

https://doi.org/10.1021/acsami.2c06546
ACS Appl. Mater. Interfaces 2022, 14, 27686−27702

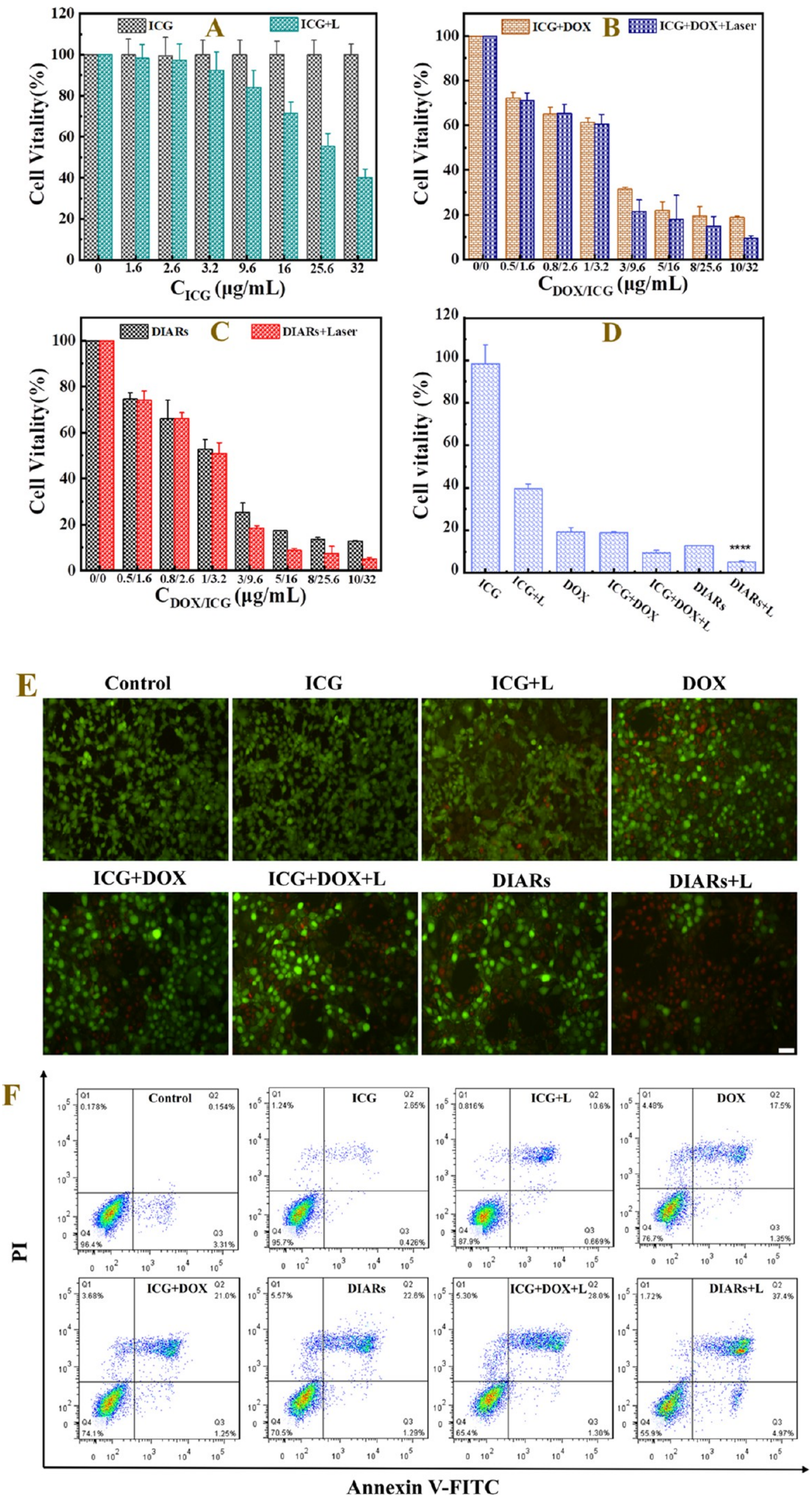

Figure 6. continued

https://doi.org/10.1021/acsami.2c06546
ACS Appl. Mater. Interfaces 2022, 14, 27686−27702

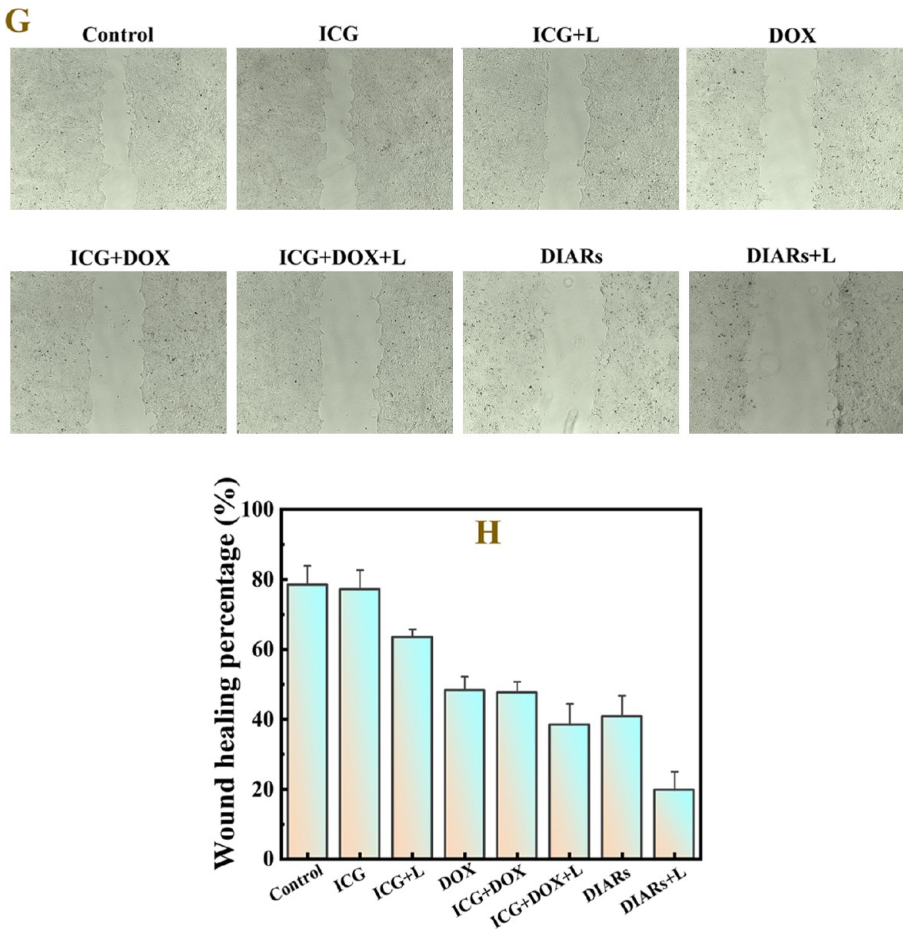

Figure 6. Cytotoxicity of DIARs evaluated by the MTT assay. (A) Cytotoxicity of ICG at different concentrations with or without laser irradiation. (B) Cytotoxicity of ICG + DOX at different concentrations with or without laser irradiation. (C) Cytotoxicity of DIARs at different concentrations with or without laser irradiation. (D) Cytotoxicity of each group at the DOX and ICG concentrations of 10 and 32 μg/mL, respectively. (E) Cytotoxicity of each group investigated by Calcein AM/propidium iodide (PI) staining. Scale bar is 100 μm. (F) Apoptosis assay analyzed by annexin V and PI on flow cytometry. (G) Migration of cells after different treatments was imaged with an optical microscope. Scale bar is 200 μm. (H) Wound healing percentage of each treated group calculated by ImageJ. Data in (A–D) and (H) are represented as mean values ± SD, $n = 3$. Statistical differences were analyzed by a two-tailed Student's t-test. ****$p < 0.0001$.

after irradiation. Subsequent investigation showed that the effect of ICG + DOX on 4T1 cells was similar to that of free DOX, but with laser irradiation (ICG + DOX + L), the cytotoxicity was further elevated, suggesting ICG and DOX had synergistic cytotoxicity under irradiation (Figure 6B). After determining the cytotoxicity of each free drug in monotherapy and combination therapy, the effect of DIARs and DIARs + L was evaluated. In line with our expectations, the cells treated with DIARs + L showed considerably enhanced cytotoxicity compared with the other six groups (Figure 6C). Meanwhile, as shown in Table S2, the combination index (CI) of the DIARs + L-treated group was 3.14 times smaller than that of the ICG + DOX + L group (CI values < 1 indicated synergism of the two drugs, the smaller CI values indicated the higher synergism). Figure 6D shows the integrated diagram showing the cell viability of each group (at 10 μg/mL DOX and 32 μg/mL ICG). Obviously, DIARs + L showed significantly higher cytotoxicity than other groups. Owing to the EPR effect of gADNVs and the targeting capability of RGD, the increase of cellular uptake of DIARs promoted the killing of cells.

The cytotoxicity of DIARs combined with NIR laser irradiation was further investigated by Calcein AM/propidium iodide (PI) staining.[56] As shown in Figure 6E, prominent green fluorescence (live cell staining) was observed in the PBS and ICG groups without irradiation. In contrast, those with irradiation showed varying degrees of red fluorescence (dead cells staining), and the number of live cells decreased extensively. Especially, DIARs plus irradiation (DIARs + L) group had dramatic cell damage, showing a large number of red-stained cells. In addition, Annexin V/PI staining analysis also showed the same tendency that DIARs + L induced significantly more late apoptosis/necrosis cells as compared with other groups (Figure 6F). These outcomes indicated that DIARs combined with NIR laser irradiation were an effective nanosystem for the combinational photochemotherapy of breast cancer.

Additionally, tumor metastasis is also an obstacle in cancer therapy, and it significantly affects the therapeutic efficiency, clinical curative rate, and prognosis of cancer.[3] To evaluate the *in vitro* antimetastatic effect of DIARs, the scratch assay was performed. As shown in Figure 6G, the 4T1 cells had obvious metastatic behavior in the negative control group (cells were cultured in RPMI medium without medical intervention), while the other groups exhibited varying degrees of inhibition to the metastasis of 4T1 cells. Compared with free ICG-, ICG

https://doi.org/10.1021/acsami.2c06546
ACS Appl. Mater. Interfaces 2022, 14, 27686−27702

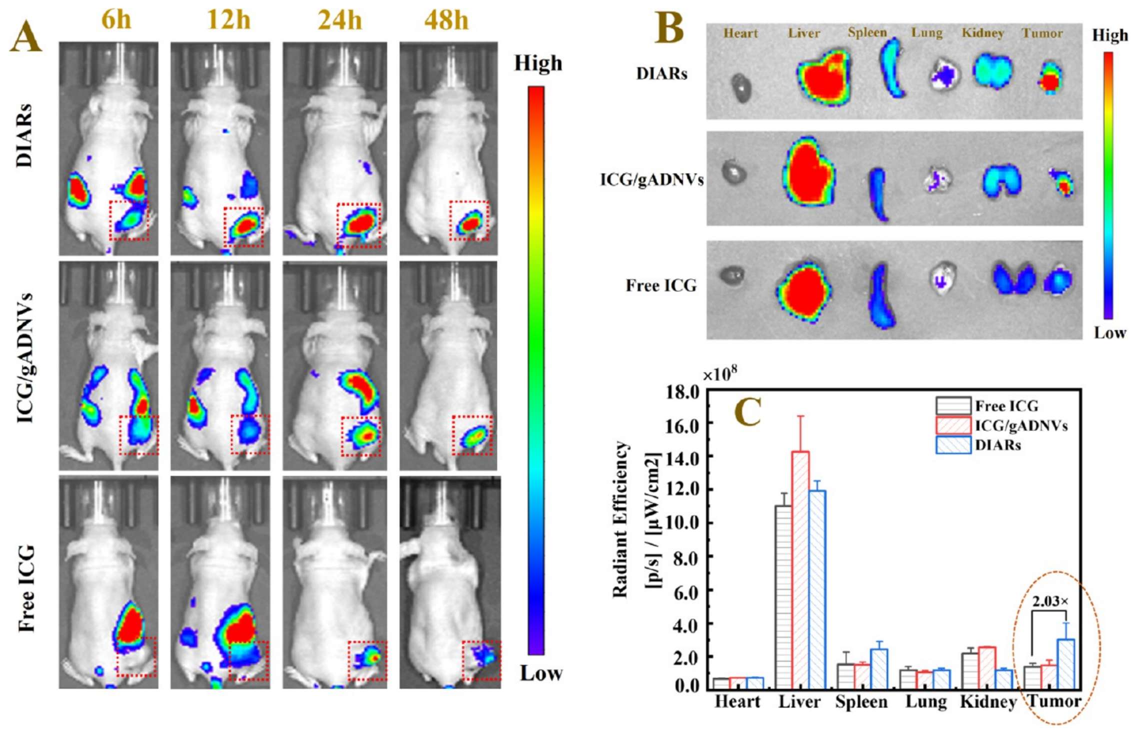

Figure 7. Biodistribution of DIARs in *in vivo* study. (A) Biodistribution of *in vivo* ICG, ICG/gADNVs, and DIARs analyzed at 6, 12, 24, and 48 h. (B) Image of organs (including the heart, liver, spleen, lung, and kidney) and tumors of each group at 48 h post injection. (C) Radiant efficiency of organs (including the heart, liver, spleen, lung, and kidney) and tumors of each group at 48 h post injection. Data in (C) are represented as mean values ± SD, n = 3.

+ L-, ICG + DOX-, ICG + DOX + L- and DIARs-treated groups, the cells treated with DIARs + L showed the most inhibition of metastasis. As shown in Figure 6H, the metastatic potential decreased from 78.5% (negative control group) to 19.7% (DIARs + L-treated group). This result suggested that aside from the induced tumor cell apoptosis, DIARs combined with NIR laser irradiation inhibited the proliferation and migration of tumor cells, allowing effective cancer therapy with fewer concerns about metastasis.

3.5. *In Vivo* Targeted Delivery Study. ICG as a commonly adopted NIR probe was used for monitoring the distribution of DIARs *in vivo*. To explore the targeted effect of RGD and the enrichment and protective effect of gADNVs, the real-time distributions of free ICG, ICG/gADNVs, and DIARs were monitored in the 4T1 mammary tumor model. As shown in Figure 7A, the fluorescence signals of ICG/gADNVs and DIARs were observed in the tumor tissue after 6 h of injection, but no signal of free ICG was observed. Also, the fluorescence intensity was increased as time prolonged. Particularly, the mice models injected with DIARs showed increasing fluorescence and reached their peak at 24 h post injection. The fluorescence intensity of each group showed a tendency of DIARs > ICG/gADNVs > free ICG. Compared with the fluorescent signal of ICG/gADNVs, the signal of free ICG was cleared significantly within 12−24 h. After 48 h, the organs (including heart, liver, spleen, lung, and kidney) and tumors of each group were separated from mice for the monitoring of fluorescence. As shown in Figure 7B,C, tumors in the DIARs-treated group showed more fluorescence retention than the other two groups (Figure 7B), and the radiant efficiency was 2.03-fold of that in the free ICG treat group (Figure 7C). These results suggested that gADNVs as carriers could avoid rapid degradation or premature excretion of drugs and might facilitate its accumulation in tumors. The modification of RGD onto gADNVs further elevated the tumor-targeted performance, resulting in an increased tumor accumulation as well. Therefore, DIARs with the desired performances including long circulation and efficient tumor accumulation had great potential for cancer therapy.

3.6. *In Vivo* Antitumor Evaluation. On the basis of the *in vivo* distribution, cell uptake, and cytotoxicity results, the *in vivo* antitumor effect of DIARs was evaluated in 4T1 tumor-bearing mice models. First, the *in vivo* photothermal experiments were observed after intravenously injecting PBS, DOX, ICG, ICG + DOX, and DIARs into mice. At 24 h post injection, the 808 nm NIR laser was applied above the tumor for 5 min irradiation. The temperature and photothermal images of the mice were captured with an infrared thermal camera. As shown in Figure 8A, the temperature in the tumor sites treated with PBS and DOX exhibited only slight warming (increased to about 40 °C). The free ICG- or free ICG + DOX-treated mice resulted in an increase of the tumor temperature to about 44 °C, which suggested ICG could be ingested into the tumor site during circulation. More remarkably, the mice treated with DIARs showed the most temperature increase up to 46.4 °C at the tumor site (about 13−14 °C increase), which was higher than the effective temperature for tumor ablation (42 °C).[57] Therefore, the DIARs-treated mice upon laser irradiation exhibited effective PTT effects, indicating that gADNVs as carriers modified with RGD could efficiently enhance drug delivery and tumor therapy efficiency.

Next, the *in vivo* antitumor effect of PBS, DOX, ICG, ICG + L, ICG + DOX, ICG + DOX + L, DIARs, and DIARs + L was evaluated *via* intravenously injecting every other day for 14 days (Figure 8B). The tumor growth was monitored and is

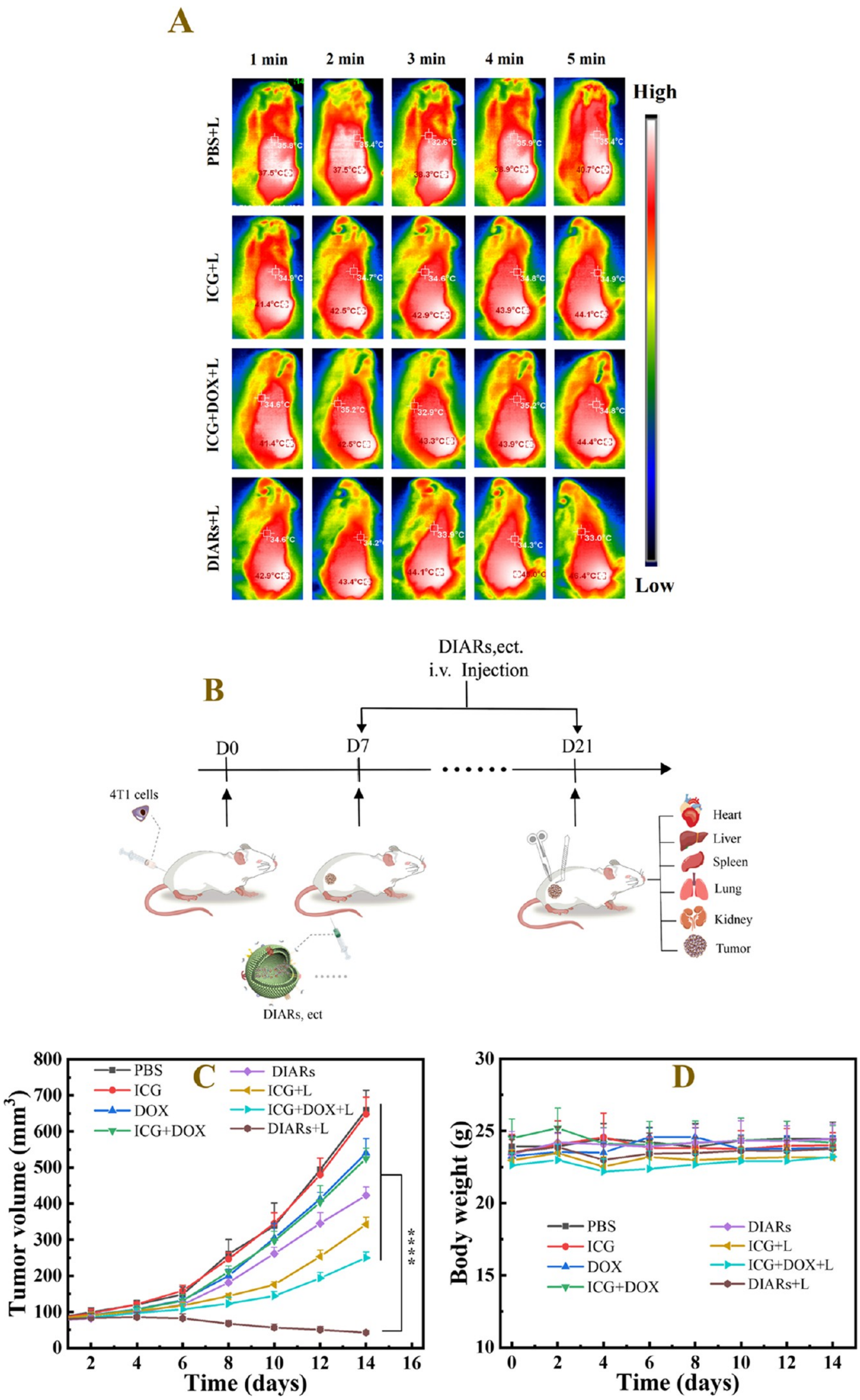

Figure 8. continued

https://doi.org/10.1021/acsami.2c06546
ACS Appl. Mater. Interfaces 2022, 14, 27686−27702

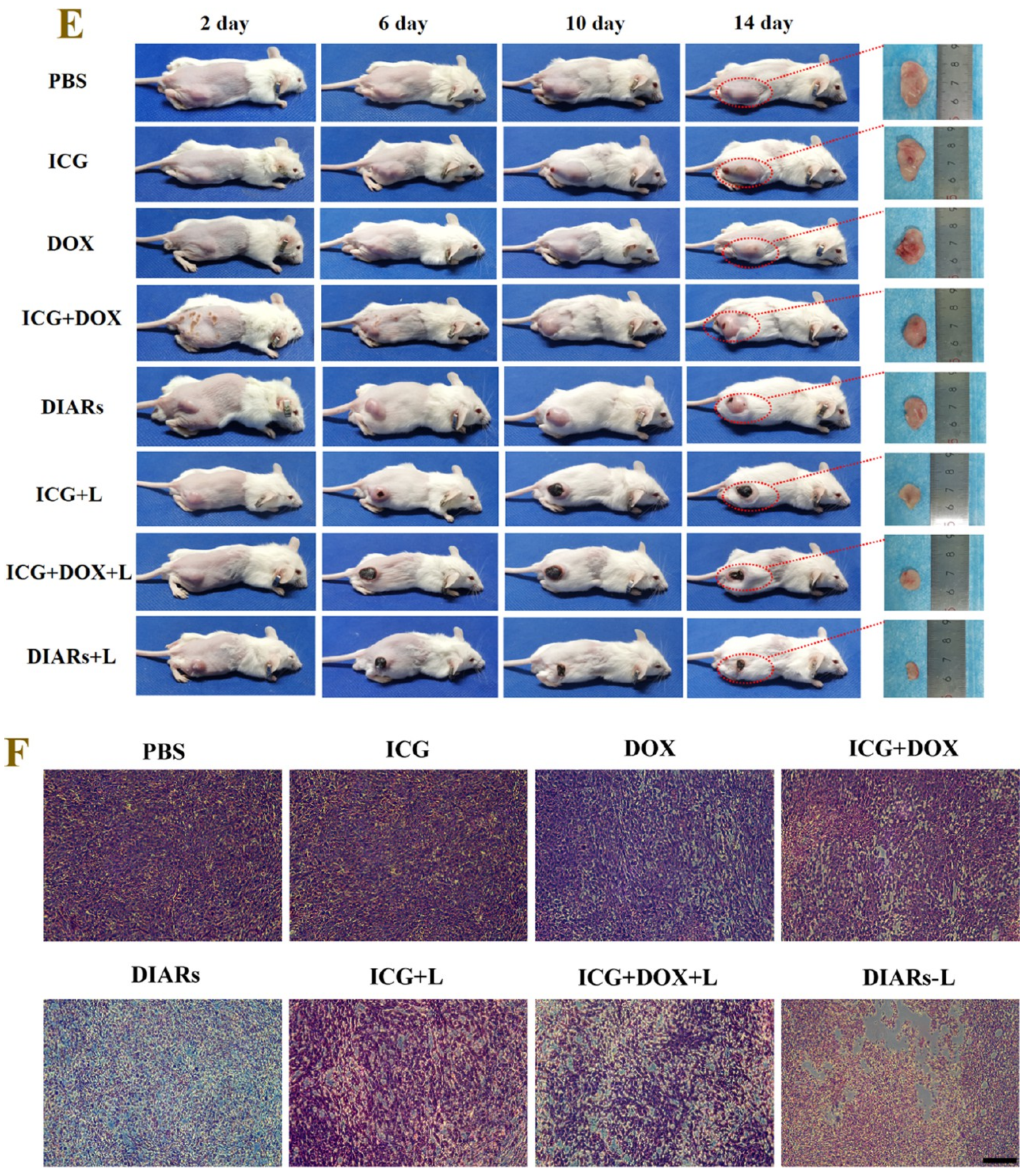

Figure 8. (A) Temperature and photothermal images of the mice captured with an infrared thermal camera. The temperature shown in white is the body temperature of the mouse, and the temperature shown in red is the temperature after laser irradiation. (B) Flow chart of administration in mice. (C) Tumor growth curve of each group during treatment. (D) Body weight of each group during treatment. (E) Diagram of tumor changes in mice during treatment. (F) H&E staining of tumors of each group; scale bar is 100 μm. Data in (C) and (D) are represented as mean values ± SD, n = 3. Statistical differences were analyzed by a two-tailed Student's t-test. ****p < 0.0001.

presented in Figure 8E,C. The tumors treated with PBS + L and ICG showed similar growth trends and increased rapidly during treatment. Free DOX or ICG + DOX only slightly inhibited tumor growth after seven treatments, whereas the DIARs-injected mice showed more inhibition of tumor growth than free DOX. It is worth noting that with NIR irradiation, like in ICG + L, ICG + DOX + L, and DIARs + L groups, the inhibition is more considerable. Nevertheless, the combination of ICG and DOX under NIR irradiation was not enough to eradicate the tumor growth, presumably due to the degradation and clearance of free drugs by enzymes or the immune system in the blood before they arrived at the tumor site. Remarkably, the tumor sizes were inhibited or even shrunk after treatment with DIARs + L. We accredited the result to the alliance from the protection by gADNVs, the targeted delivery of RGD, and the therapeutic action of ICG and DOX, which led to efficient drug delivery and target therapy. Likewise, hematoxylin−eosin (H&E) staining of tumors showed cell damage at a tendency of DIARs + L > ICG + DOX + L > ICG + L > DIARs > ICG + DOX ≈ DOX > ICG ≈ PBS (Figure 8F), although other organs exhibited no obvious lesion or tumor metastasis (Figure S6). The body weights of mice had no distinct change during treatment (Figure 8D), indicating that our treatment did not cause apparent damage to the growth of mice. These results overall revealed that our prepared DIARs, assisted with tumor-targeted RGD and efficient dual loading of ICG and DOX in gADNVs, were promising to be effective and safe NDDSs for tumor treatment.

4. CONCLUSIONS

In summary, we, for the first time, successfully utilized the $\pi-\pi$ stacking interaction between ICG and DOX to prepare a gADNV-based nanosystem with high drug loading efficiency and great stability. This nanosystem further was modified with a tumor-targeted peptide (RGD), exhibiting 4T1 cell targeting characteristics and specific tumor accumulation. Moreover, we demonstrated that the well-formed DIARs under NIR laser irradiation induced an efficient synergy of phototherapy and chemotherapy. Upon the amalgamation of two therapies, rather than relying on a single drug, DIARs showed great cytotoxicity and antimetastatic effect. By constitutively integrating the natural and economical gADNVs, the $\pi-\pi$ stacking interaction-based on efficient drug loading and tumor-targeted RGD modification, our DIARs are expected to serve as a promising NDDS for the growing demand for effective tumor-targeted drug delivery and efficient cancer treatment.

■ ASSOCIATED CONTENT

Supporting Information

The Supporting Information is available free of charge at https://pubs.acs.org/doi/10.1021/acsami.2c06546.

> Method of gADNV isolation and characterization; DSPE-PEG-RGD insertion of gADNVs; the TEM image of DIARs after 808 nm laser irradiation; the particle size change of DIARs analyzed by DLS for 10 days when stored in PBS, H_2O, and RPMI 1640 culture media; the enlarged picture of cells treated with DIARs for 2 h; the intracellular ROS level in different treating groups investigated by flow cytometry using DCFH-DA as the fluorescent probe; the cytotoxicity of DOX evaluated by the MTT assay; the H&E staining of tumors of each group; the electronic energies of DOX′ and ICG′ and the calculation of binding energy (E_b); the CI of ICG + DOX + L or DIARs in different concentrations and the Cartesian coordinates of DOX′, ICG′, and complex (PDF)

■ AUTHOR INFORMATION

Corresponding Authors

Xi Zhang − *The School of Pharmacy, Fujian Medical University, Fuzhou, Fujian 350122, P. R. China; Fujian Key Laboratory of Drug Target Discovery and Structural and Functional Research, The School of Pharmacy, Fujian Medical University, Fuzhou, Fujian 350122, P. R. China*; Email: xz@fjmu.edu.cn

Jing Zhang − *Department of Chemical Biology, College of Life Sciences, Fujian Agriculture and Forestry University, Fuzhou, Fujian 350002, P. R. China*; Email: 517674177@qq.com

Jinghua Chen − *The School of Pharmacy, Fujian Medical University, Fuzhou, Fujian 350122, P. R. China; Fujian Key Laboratory of Drug Target Discovery and Structural and Functional Research, The School of Pharmacy, Fujian Medical University, Fuzhou, Fujian 350122, P. R. China*; orcid.org/0000-0001-8718-0232; Email: cjh_huaxue@126.com

Authors

Lupeng Zeng − *The School of Pharmacy, Fujian Medical University, Fuzhou, Fujian 350122, P. R. China; Fujian Key Laboratory of Drug Target Discovery and Structural and Functional Research, The School of Pharmacy, Fujian Medical University, Fuzhou, Fujian 350122, P. R. China*

Wanhua Shi − *The School of Pharmacy, Fujian Medical University, Fuzhou, Fujian 350122, P. R. China; Fujian Key Laboratory of Drug Target Discovery and Structural and Functional Research, The School of Pharmacy, Fujian Medical University, Fuzhou, Fujian 350122, P. R. China*

Huaying Wang − *The School of Pharmacy, Fujian Medical University, Fuzhou, Fujian 350122, P. R. China; Fujian Key Laboratory of Drug Target Discovery and Structural and Functional Research, The School of Pharmacy, Fujian Medical University, Fuzhou, Fujian 350122, P. R. China*

Xin Cheng − *The School of Pharmacy, Fujian Medical University, Fuzhou, Fujian 350122, P. R. China; Fujian Key Laboratory of Drug Target Discovery and Structural and Functional Research, The School of Pharmacy, Fujian Medical University, Fuzhou, Fujian 350122, P. R. China*

Tingting Chen − *The School of Pharmacy, Fujian Medical University, Fuzhou, Fujian 350122, P. R. China; Fujian Key Laboratory of Drug Target Discovery and Structural and Functional Research, The School of Pharmacy, Fujian Medical University, Fuzhou, Fujian 350122, P. R. China*

Liang liang Wang − *The School of Pharmacy, Fujian Medical University, Fuzhou, Fujian 350122, P. R. China; Fujian Key Laboratory of Drug Target Discovery and Structural and Functional Research, The School of Pharmacy, Fujian Medical University, Fuzhou, Fujian 350122, P. R. China*

Jianming Lan − *The School of Pharmacy, Fujian Medical University, Fuzhou, Fujian 350122, P. R. China; Fujian Key Laboratory of Drug Target Discovery and Structural and Functional Research, The School of Pharmacy, Fujian Medical University, Fuzhou, Fujian 350122, P. R. China*

Weiming Sun − *The School of Pharmacy, Fujian Medical University, Fuzhou, Fujian 350122, P. R. China; Fujian Key Laboratory of Drug Target Discovery and Structural and Functional Research, The School of Pharmacy, Fujian Medical University, Fuzhou, Fujian 350122, P. R. China*; orcid.org/0000-0002-9882-0511

Meicen Liu − *Longyan First Affiliated Hospital of Fujian Medical University, Fujian Medical University, Longyan, Fujian 364000, P. R. China*

Complete contact information is available at: https://pubs.acs.org/10.1021/acsami.2c06546

Notes

The authors declare no competing financial interest.

■ ACKNOWLEDGMENTS

Funding: This work was supported by the innovation of Science and Technology, Fujian province [grant no: 2019Y9008], Natural Science Foundation of Fujian Province [grant nos: 2020J01545, 2020Y0022, 2019J01614], Startup Fund for Scientific Research, Fujian Medical University [grant nos: 2018QH2022, 2018QH2015] and Science and Technology Plan Project of Longyan [grant no: 2018LYF8017]. The authors gratefully acknowledge the technical assistance of Cailing Yan, Linying Zhou, and Zhihong Huang from the Public Technology Service Center (Fujian Medical University) for their technical assistance.

■ ABBREVIATIONS

gADNVs, aloe gel-derived nanovesicles
RGD, Arg-Gly-Asp, integrin-targeted peptide
ICG, indocyanine green
DOX, doxorubicin
DIARs, RGD-modified gADNVs loaded with ICG and DOX
PTT, photothermal therapy

NDDSs, nanocarrier-based drug delivery systems
ICG/gADNVs, gADNVs loaded with indocyanine
EPR, enhanced permeability and retention
PDNVs, plant-derived nanovesicles
PA, phosphatidic acid
DFT, density functional theory
PBS, phosphate buffer
DLS, dynamic light scattering
TEM, transmission electron microscopy

■ REFERENCES

(1) Yu, W.; Hu, C.; Gao, H. Advances of Nanomedicines in Breast Cancer Metastasis Treatment Targeting Different Metastatic Stages. *Adv. Drug Delivery Rev.* **2021**, *178*, No. 113909.

(2) Chaffer, C. L.; Weinberg, R. A Perspective on Cancer Cell Metastasis. *Science* **2011**, *331*, 1559−1564.

(3) Liu, X.; Wang, C.; Ma, H.; Yu, F.; Hu, F.; Yuan, H. Water-Responsive Hybrid Nanoparticles Codelivering ICG and DOX Effectively Treat Breast Cancer via Hyperthermia-aided DOX Functionality and Drug Penetration. *Adv. Healthcare Mater.* **2019**, *8*, No. e1801486.

(4) Chen, Z.; Wang, W.; Li, Y.; Wei, C.; Zhong, P.; He, D.; Liu, H.; Wang, P.; Huang, Z.; Zhu, W.; Zhou, Y.; Qin, L. Folic Acid-Modified Erythrocyte Membrane Loading Dual Drug for Targeted and Chemo-Photothermal Synergistic Cancer Therapy. *Mol. Pharmaceutics* **2021**, *18*, 386−402.

(5) Li, Q.; Li, W.; Di, H.; Luo, L.; Zhu, C.; Yang, J.; Yin, X.; Yin, H.; Gao, J.; Du, Y.; You, J. A Photosensitive Liposome with NIR Light Triggered Doxorubicin Release as a Combined Photodynamic-chemo Therapy System. *J. Controlled Release* **2018**, *277*, 114−125.

(6) Yu, L.; Dong, A.; Guo, R.; Yang, M.; Deng, L.; Zhang, J. DOX/ICG Coencapsulated Liposome-Coated Thermosensitive Nanogels for NIR-Triggered Simultaneous Drug Release and Photothermal Effect. *ACS. Biomater. Sci. Eng.* **2018**, *4*, 2424−2434.

(7) Cheng, X.; Gao, J.; Ding, Y.; Lu, Y.; Wei, Q.; Cui, D.; Fan, J.; Li, X.; Zhu, E.; Lu, Y.; Wu, Q.; Li, L.; Huang, W. Multi-Functional Liposome: A Powerful Theranostic Nano-Platform Enhancing Photodynamic Therapy. *Adv. Sci.* **2021**, *8*, No. e2100876.

(8) Deng, X.; Shao, Z.; Zhao, Y. Solutions to the Drawbacks of Photothermal and Photodynamic Cancer Therapy. *Adv. Sci.* **2021**, *8*, No. 2002504.

(9) Wan, G.; Chen, B.; Li, L.; Wang, D.; Shi, S.; Zhang, T.; Wang, Y.; Zhang, L.; Wang, Y. Nanoscaled Red Blood Cells Facilitate Breast Cancer Treatment by Combining Photothermal/photodynamic Therapy and Chemotherapy. *Biomaterials* **2018**, *155*, 25−40.

(10) Liu, Y.; Ai, K.; Liu, J.; Deng, M.; He, Y.; Lu, L. Dopamine-melanin Colloidal Nanospheres: An Efficient Near-infrared Photothermal Therapeutic Agent for *in vivo* Cancer Therapy. *Adv. Mater.* **2013**, *25*, 1353−1359.

(11) Minko, T.; Rodriguez-Rodriguez, L.; Pozharov, V. Nanotechnology Approaches for Personalized Treatment of Multidrug Resistant Cancers. *Adv. Drug Delivery Rev.* **2013**, *65*, 1880−1895.

(12) Majumder, J.; Taratula, O.; Minko, T. Nanocarrier-based Systems for Targeted and Site Specific Therapeutic Delivery. *Adv. Drug Delivery Rev.* **2019**, *144*, 57−77.

(13) Su, C.; Liu, Y.; Li, R.; Wu, W.; Fawcett, J.-P.; Gu, J. Absorption, Distribution, Metabolism and Excretion of the Biomaterials Used in Nanocarrier Drug Delivery Systems. *Adv. Drug Delivery Rev.* **2019**, *143*, 97−114.

(14) Yi, H.; Lu, W.; Liu, F.; Zhang, G.; Xie, F.; Liu, W.; Wang, L.; Zhou, W.; Cheng, Z. ROS-responsive Liposomes with NIR Light-triggered Doxorubicin Release for Combinatorial Therapy of Breast Cancer. *J. Nanobiotechnol.* **2021**, *19*, No. 134.

(15) Zhu, D.; Fan, F.; Huang, C.; Zhang, Z.; Qin, Y.; Lu, L.; Wang, H.; Jin, X.; Zhao, H.; Yang, H.; Zhang, C.; Yang, J.; Liu, Z.; Sun, H.; Leng, X.; Kong, D.; Zhang, L. Bubble-generating Polymersomes Loaded with Both Indocyanine Green and Doxorubicin for Effective Chemotherapy Combined with Photothermal Therapy. *Acta. Biomater.* **2018**, *75*, 386−397.

(16) Sun, Q.; You, Q.; Wang, J.; Liu, L.; Wang, Y.; Song, Y.; Cheng, Y.; Wang, S.; Tan, F.; Li, N. Theranostic Nanoplatform: Triple-Modal Imaging-Guided Synergistic Cancer Therapy Based on Liposome-Conjugated Mesoporous Silica Nanoparticles. *ACS. Appl. Mater. Interfaces* **2018**, *10*, 1963−1975.

(17) Luther, D.-C.; Huang, R.; Jeon, T.; Zhang, X.; Lee, Y.-W.; Nagaraj, H.; Rotello, V.-M. Delivery of Drugs, Proteins, and Nucleic Acids Using Inorganic Nanoparticles. *Adv. Drug Delivery Rev.* **2020**, *156*, 188−213.

(18) Zhang, N.; Li, M.; Sun, X.; Jia, H.; Liu, W. NIR-responsive Cancer Cytomembrane-cloaked Carrier-free Nanosystems for Highly Efficient and Self-Targeted Tumor Drug Delivery. *Biomaterials* **2018**, *159*, 25−36.

(19) Yang, C.; Zhang, M.; Merlin, D. Advances in Plant-derived Edible Nanoparticle-based lipid Nano-drug Delivery Systems as Therapeutic Nanomedicines. *J. Mater. Chem. B* **2018**, *6*, 1312−1321.

(20) Wang, Q.; Zhuang, X.; Mu, J.; Deng, Z.-B.; Jiang, H.; Zhang, L.; Xiang, X.; Wang, B.; Yan, J.; Miller, D.; Zhang, H.-G. Delivery of Therapeutic Agents by Nanoparticles Made of Grapefruit-derived Lipids. *Nat. Commun.* **2013**, *4*, No. 1867.

(21) Dad, H.-A.; Gu, T.-W.; Zhu, A.-Q.; Huang, L.-Q.; Peng, L. H. Plant Exosome Like Nanovesicles: Emerging Therapeutics and Drug Delivery Nanoplatforms. *Mol. Ther.* **2021**, *29*, 13−31.

(22) Sarvarian, P.; Samadi, P.; Gholipour, E.; Shams Asenjan, K.; Hojjat-Farsangi, M.; Motavalli, R.; Motavalli Khiavi, F.; Yousefi, M. Application of Emerging Plant-Derived Nanoparticles as a Novel Approach for Nano-Drug Delivery Systems. *Immunol. Invest.* **2021**, *51*, 1−21.

(23) Iravani, S.; Varma, R.-S. Plant-derived Edible Nanoparticles and miRNAs: Emerging Frontier for Therapeutics and Targeted Drug-delivery. *ACS Sustainable Chem. Eng.* **2019**, *7*, 8055−8069.

(24) Teng, Y.; Ren, Y.; Sayed, M.; Hu, X.; Lei, C.; Kumar, A.; Hutchins, E.; Mu, J.; Deng, Z.; Luo, C.; Sundaram, K.; Sriwastva, M.-K.; Zhang, L.; Hsieh, M.; Reiman, R.; Haribabu, B.; Yan, J.; Jala, V.-R.; Miler, D.-M.; Van Keuren-Jensen, K.; Merchant, M.-L.; McClain, C.-J.; Park, J.-W.; Egilmerz, N.-K.; Zhang, H.-G. Plant-derived Exosomal microRNAs Shape the Gut Microbiota. *Cell Host Microbe* **2018**, *24*, 637−652.e8.

(25) Sundaram, K.; Miller, D.-P.; Kumar, A.; Teng, Y.; Sayed, M.; Mu, J.; Lei, C.; Sriwastva, M.-K.; Zhang, L.; Yan, J.; Merchant, M.-L.; He, L.; Fang, Y.; Zhang, S.; Zhang, X.; Park, J.-W.; Lamont, R.-J.; Zhang, H.-G. Plant-Derived Exosomal Nanoparticles Inhibit Pathogenicity of Porphyromonas gingivalis. *iScience* **2019**, *21*, 308−327.

(26) Niu, W.; Xiao, Q.; Wang, X.; Zhu, J.; Li, J.; Liang, X.; Peng, Y.; Wu, C.; Lu, R.; Pan, Y.; Luo, J.; Zhong, X.; He, H.; Rong, Z.; Fan, J.-B.; Wang, Y. A Biomimetic Drug Delivery System by Integrating Grapefruit Extracellular Vesicles and Doxorubicin-Loaded Heparin-Based Nanoparticles for Glioma Therapy. *Nano. Lett.* **2021**, *21*, 1484−1492.

(27) Zeng, L.; Wang, H.; Shi, W.; Chen, L.; Chen, T.; Chen, G.; Wang, W.; Lan, J.; Huang, Z.; Zhang, J.; Chen, J. Aloe Derived Nanovesicle as a Functional Carrier for Indocyanine Green Encapsulation and Phototherapy. *J. Nanobiotechnol.* **2021**, *19*, No. 439.

(28) Zucker, D.; Marcus, D.; Barenholz, Y.; Goldblum, A. Liposome Drugs' Loading Efficiency: A Working Model based on Loading Conditions and Drug's Physicochemical Properties. *J. Controlled Release* **2009**, *139*, 73−80.

(29) Lin, L.; Liang, X.; Xu, Y.; Yang, Y.; Li, X.; Dai, Z. Doxorubicin and Indocyanine Green Loaded Hybrid Bicelles for Fluorescence Imaging Guided Synergetic Chemo/Photothermal Therapy. *Bioconjugate Chem.* **2017**, *28*, 2410−2419.

(30) Wei, X.; Wang, Y.; Xiong, X.; Guo, X.; Zhang, L.; Zhang, X.; Zhou, S. Codelivery of a π-π Stacked Dual Anticancer Drug Combination with Nanocarriers for Overcoming Multidrug Resistance and Tumor Metastasis. *Adv. Funct. Mater.* **2016**, *26*, 8266−8280.

https://doi.org/10.1021/acsami.2c06546
ACS Appl. Mater. Interfaces 2022, 14, 27686−27702

(31) Frisch, M.-J.; Trucks, G.-W.; Schlegel, H.-B.; Scuseria, G.-E.; Robb, M.-A.; Cheeseman, J.-R.; Scalmani, G.; Barone, V.; Mennucci, B.; Petersson, G.-A.; Nakatsuji, H.; Caricato, M.; Li, X.; Hratchian, H.-P.; Izmaylov, A.-F.; Bloino, G.-Z.-J.; Sonnenberg, J.-L.; Hada, M.; Ehara, M.; Toyota, K.; Fukuda, R.; Hasegawa, J.; Ishida, M.; Nakajima, T.; Honda, Y.; Kitao, O.; Nakai, H.; Vreven, T.; Montgomery, J.-A.; Peralta, J.-E.; Ogliaro, F.; Bearpark, M.; Heyd, J.-J.; Brothers, E.; Kudin, K.-N.; Staroverov, V.-N.; Keith, T.; Kobayashi, R.; Normand, J.; Raghavachari, K.; Rendell, A.; Burant, J. C.; Iyengar, S. S.; Tomasi, J.; Cossi, M.-N.; Rega, J.-M.; Millam, M.; Klene, J. E.; Knox, J. B.; Cross, V.; Bakken, C.; Adamo, J.; Jaramillo, R.; Gomperts, R.-E.; Stratmann, O.; Yazyev, A. J.; Austin, R.; Cammi, C.; Pomelli, J.-W.; Ochterski, R.-L.; Martin, K.; Morokuma, V.-G.; Zakrzewski, G.-A.; Voth, P.; Salvador, J.-J.; Dannenberg, S.; Dapprich, A.-D.; Daniels, O.; Farkas, J.-B.; Foresman, J.-V.; Ortiz, J.; Cioslowski, D.-J. Fox. *Gaussian 16* revision A.03; Gaussian, Inc.: Wallingford, CT, 2016.

(32) Grimme, S.; Ehrlich, S.; Goerigk, L. Effect of the Damping Function in Dispersion Corrected Density Functional Theory. *J. Comput. Chem.* **2011**, *32*, 1456−1465.

(33) Marenich, A.-V.; Cramer, C.-J.; Truhlar, D.-G. Universal Solvation Model based on Solute Electron Density and on a Continuum Model of the Solvent Defined by the Bulk Dielectric Constant and Atomic Surface Tensions. *J. Phys. Chem. B* **2009**, *113*, 6378−6396.

(34) Dennington, R.-D., II.; Keith, T.-A.; Millam, J.-M. *GaussView*, version 6; Semichem Inc.: Shawnee Mission, KS, 2016.

(35) Hwang, J.-W.; Li, P.; Shimizu, K.-D. Synergy Between Experimental and Computational Studies of Aromatic Stacking Interactions. *Org. Biomol. Chem.* **2017**, *15*, 1554−1564.

(36) Zhuang, W.-R.; Wang, Y.; Cui, P.-F.; Xing, L.; Lee, J.; Kim, D.; Jiang, H.-L.; Oh, Y.-K. Applications of π-π Stacking Interactions in the Design of Drug-delivery Systems. *J. Controlled Release* **2019**, *294*, 311−326.

(37) Yang, D.; Gao, S.; Fang, Y.; Lin, X.; Jin, X.; Wang, X.; Ke, L.; Shi, K. The π-π Stacking-guided Supramolecular Self-assembly of Nanomedicine for Effective Delivery of Antineoplastic Therapies. *Nanomedicine* **2018**, *13*, 3159−3177.

(38) Chountoulesi, M.; Naziris, N.; Pippa, N.; Demetzos, C. The Significance of Drug-to-lipid Ratio to the Development of Optimized Liposomal Formulation. *J. Liposome Res.* **2018**, *28*, 249−258.

(39) Maritim, S.; Boulas, P.; Lin, Y. Comprehensive Analysis of Liposome Formulation Parameters and their Influence on Encapsulation, Stability and Drug Release in Glibenclamide Liposomes. *Int. J. Pharm.* **2021**, *592*, No. 120051.

(40) Chen, C.; Tao, R.; Ding, D.; Kong, D.; Fan, A.; Wang, Z.; Zhao, Y. Ratiometric Co-delivery of Multiple Chemodrugs in a Single Nanocarrier. *Eur. J. Pharm. Sci.* **2017**, *107*, 16−23.

(41) Göke, K.; Bunjes, H. Parameters Influencing the Course of Passive Drug Loading into Lipid Nanoemulsions. *Eur. J. Pharm. Sci.* **2018**, *126*, 123−131.

(42) Rosenblatt, K.-M.; Bunjes, H. Evaluation of the Drug Loading Capacity of Different Lipid Nanoparticle Dispersions by Passive Drug loading. *Eur. J. Pharm. Sci.* **2017**, *117*, 49−59.

(43) Göke, K.; Bunjes, H. Carrier Characteristics Influence the Kinetics of Passive Drug Loading into Lipid Nanoemulsions. *Eur. J. Pharm. Sci.* **2018**, *126*, 132−139.

(44) Wang, R.; Xiao, R.; Zeng, Z.; Xu, L.; Wang, J. Application of Poly (ethylene glycol)-distearoylphosphatidylethanolamine (PEG-DSPE) Block Copolymers and their Derivatives as Nanomaterials in Drug Delivery. *Int. J. Nanomed.* **2012**, *7*, 4185−4198.

(45) Yang, X.; Zhao, L.; Zheng, L.; Xu, M.; Cai, X. Polyglycerol Grafting and RGD Peptide Conjugation on MnO Nanoclusters for Enhanced Colloidal Stability, Selective Cellular Uptake and Cytotoxicity. *Colloids Surf., B* **2018**, *163*, 167−174.

(46) Zhang, N.; Li, J.; Zhang, P.; Yang, X.; Sun, C. Novel Nanoarchitecture of Arginine-glycine-aspartate Conjugated Gold Nanoparticles: A Sensitive and Selective Platform for Detecting Arachidonic Acid. *Anal. Bioanal. Chem.* **2019**, *411*, 7105−7113.

(47) Danaei, M.; Dehghankhold, M.; Ataei, S.; Hasanzadeh Davarani, F.; Javanmard, R.; Dokhani, A.; Khorasani, S.; Mozafari, M.-R. Impact of Particle Size and Polydispersity Index on the Clinical Applications of Lipidic Nanocarrier Systems. *Pharmaceutics* **2018**, *10*, 57.

(48) Ling, S.; Yang, X.; Li, C.; Zhang, Y.; Yang, H.; Chen, G.; Wang, Q. Tumor Microenvironment-Activated NIR-II Nanotheranostic System for Precise Diagnosis and Treatment of Peritoneal Metastasis. *Angew. Chem., Int. Ed.* **2020**, *59*, 7219−7223.

(49) Lajunen, T.; Nurmi, R.; Wilbie, D.; Ruoslahti, T.; Johansson, N.-G.; Korhonen, O.; Rog, T.; Bunker, A.; Ruponen, M.; Urtti, A. The Effect of Light Sensitizer Localization on the Stability of Indocyanine Green Liposomes. *J. Controlled Release* **2018**, *284*, 213−223.

(50) Ewe, A.; Schaper, A.; Barnert, S.; Schubert, R.; Temme, A.; Bakowsky, U.; Aigner, A. Storage Stability of Optimal Liposome-polyethylenimine Complexes (lipopolyplexes) for DNA or siRNA Delivery. *Acta Biomater.* **2014**, *10*, 2663−2673.

(51) Wytrwal, M.; Bednar, J.; Nowakowska, M.; Wydro, P.; Kepczynski, M. Interactions of Serum with Polyelectrolyte-stabilized Liposomes: Cryo-TEM studies. *Colloids Surf., B* **2014**, *120*, 152−159.

(52) Xiao, B.; Zhang, M.; Viennois, E.; Zhang, Y.; Wei, N.; Baker, M.-T.; Jung, Y.; Merlin, D. Inhibition of MDR1 Gene Expression and Enhancing Cellular Uptake for Effective Colon Cancer Treatment Using Dual-surface-functionalized Nanoparticles. *Biomaterials* **2015**, *48*, 147−160.

(53) Du, Y.; Chen, W.; Zheng, M.; Meng, F.; Zhong, Z. pH-Sensitive Degradable Chimaeric Polymersomes for the Intracellular Release of Doxorubicin Hydrochloride. *Biomaterials* **2012**, *33*, 7291−7299.

(54) Mlakar, M.; Cuculić, V.; Frka, S.; Gašparović, B. Copper-phospholipid Interaction at Cell Membrane Model Hydrophobic Surfaces. *Bioelectrochemistry* **2018**, *120*, 10−17.

(55) Chen, Z.; Wang, W.; Li, Y.; Wei, C.; Zhong, P.; He, D.; Liu, H.; Wang, P.; Huang, Z.; Zhu, W.; Zhou, Y.; Qin, L. Folic Acid-Modified Erythrocyte Membrane Loading Dual Drug for Targeted and Chemo-Photothermal Synergistic Cancer Therapy. *Mol. Pharmaceutics* **2021**, *18*, 386−402.

(56) Liao, X.; Zheng, Y.; Lin, Z.; Shen, Y.; Lin, H.; Liu, X.; Zhang, D.; Li, B. Self-Assembled Metallo-supramolecular Nanoflowers for NIR/acidic-triggered Multidrug Release, Long-term Tumor Retention and NIR-II Fluorescence Imaging-guided Photo-Chemotherapy. *Chem. Eng. J.* **2020**, *400*, No. 125882.

(57) Li, Y.; Xu, N.; Zhou, J.; Zhu, W.; Li, L.; Dong, M.; Yu, H.; Wang, L.; Liu, W.; Xie, Z. Facile Synthesis of a Metal−organic Framework Nanocarrier for NIR Imaging-guided Photothermal Therapy. *Biomater. Sci.* **2018**, *6*, 2918−2924.

https://doi.org/10.1021/acsami.2c06546
ACS Appl. Mater. Interfaces 2022, 14, 27686−27702